What Was Learned from Numerical Simulations of F-16XL (CAWAPI) at Flight Conditions

Arthur Rizzi*

Royal Institute of Technology KTH, SE-10044 Stockholm, Sweden

Okko Boelens†

National Aerospace Laboratory NLR, 1059 CM Amsterdam, The Netherlands

Adam Jirasek‡

Swedish Defence Research Agency FOI, SE-164 90 Stockholm, Sweden

Kenneth Badcock§

University of Liverpool, Liverpool L693GH, UK

Ten groups participating in the CAWAPI project have contributed steady and unsteady viscous simulations of a full-scale, semi-span model of the F-16XL-I aircraft at three different categories of flight Reynolds/Mach number combinations for comparison with flight-test measurements for purposes of code validation and improved understanding of the flight physics of complex interacting vortical flows. The steady-state simulations are done with several turbulence models of different complexity with no topology information required and which overcome Boussinesq-assumption problems in vortical flows. Detached-Eddy Simulation (DES) has been used to compute the unsteady flow. Common structured and unstructured grids as well as individually-adapted unstructured grids have been used. Although discrepancies are observed in the comparisons, overall reasonable agreement is demonstrated for surface pressure distribution, local skin friction and boundary velocity profiles. The physical modeling, steady or unsteady, and the grid resolution both contribute to the discrepancies observed in the comparisons with flight data, but at this time it cannot be determined how much each part contributes to the whole. Overall it can be said that the technology readiness of CFD-simulation technology for the study of vehicle performance of e.g. the F-16XL has matured since 2001 such that it can be used today with a reasonable level of confidence in practical use.

Contents

I Introduction **2**

II Codes Applied & Flight Conditions Simulated **5**

A The Standard Grids & Their Importance 8

III Comparisons — Vortical Flow, no breakdown — FCs:7,19,46 **9**

A FC7: $M_\infty = 0.304$, $\alpha = 11.89°$, $Re = 44.4\ M$ 10

B FC19: $M_\infty = 0.36$, $\alpha = 11.85°$, $Re = 46.8\ M$ 17

C FC46: $M_\infty = 0.527$, $\alpha = 10.4°$, $Re = 46.9\ M$ 18

*Professor, Department of Aeronautical & Vehicle Engineering, Associate Fellow AIAA

†R&D Engineer, Applied Computational Fluid Dynamics, Department of Flight Physics and Loads, Aerospace Vehicles Division, boelens@nlr.nl, AIAA member

‡Research Engineer, Division of Systems Technology, AIAA Member

§Professor of Computational Aerodynamics, Department of Engineering, AIAA Member

IV Comparisons — Vortex Breakdown at High α — FC25
$M_\infty = 0.242$, $\alpha = 19.8°$, $Re = 32.22\ M$ **21**
A Overall Vortical Flow Features . . . 21
B C_p Comparisons along Butt-line Sections . . . 21
C C_p Comparisons along Fuselage Stations . . . 22

V Comparisons — Transonic Effects, Low α — FC70
$M_\infty = 0.97$, $\alpha = 4.3°$, $Re = 88.8\ M$ **25**
A Overall Vortical Flow Features of FC70 . . . 25
B C_p Comparisons along Butt Line Sections . . . 26
C C_p Comparisons along along Fuselage Stations . . . 26

VI Observations & Lessons Learned **30**
A Grids & Grid Design . . . 30
B Turbulence Modeling Effects . . . 31
C Unsteady Flow Effects . . . 33

VII Progress Made in Modeling since NASA-TP[1] **33**
A Status of CFD Predictions Reported in the NASA-TP[1] . . . 33
B Progress since the NASA-TP . . . 34

Nomenclature

BL = butt line on airplane, in., positive on right wing, chordwise
CAWAP = Cranked Arrow Wing Aerodynamics Project
CAWAPI = Cranked Arrow Wing Aerodynamics Project International
C_p = static-pressure coefficient
$\mathbf{C}_f$ = $\tau_w/.5\rho {V_\infty}^2$ local skin friction coefficient, a vector
FC = Flight Condition
FS = fuselage station on airplane, in., spanwise
$\mathrm{F-16XL}$ = An extensively modified version of the F-16 aircraft which is longer and has a cranked arrow wing has a cranked arrow wing instead of a trapezoidal wing with leading-edge strake
Re = Reynolds number
V/V_{RE} = ratio of velocity magnitude in boundary layer to that at the Rake Extreme total-pressure tube
x/c = fractional distance along the local chord
y^+ = Dimensionless, sublayer-scale, distance, $u_\tau y/\nu$
$2y/b$ = fractional distance along the local semispan, positive toward the right wing tip

Organzations

DLR = German Aerospace Center / Germany
$\mathrm{EADS-MAS}$ = European Aeronautics and Defence Company - Military Aircraft Systems / Germany
FOI = Swedish Defence Reseacrh Agency / Sweden
KTH = Royal Institute of Technology / Sweden
LMAC = Lockheed Martin Aeronautics Company / USA
NASA = National Aeronautics and Space Agministration / USA
NLR = National Aerospace Laboratory / Netherlands
ULiv = University of Liverpool / UK
UTSimC = University of Tennessee at Chattanooga / USA
USAFA = United States Airforce Academy / USA

I. Introduction

The RTO-AVT-113 working group was established under a Technical Activity Programme (TAP) and Terms of Reference (TOR). The TAP defined the purpose of the working group as the validation of CFD for unsteady vortical flows through carefully coordinated experiments to help identify modeling weaknesses and best practices, resulting in improved understanding and prediction of aircraft aerodynamic characteristics prior to full-scale fabrication. The motivation for this is to reduce testing, and hence cost, required during the development of future military aircraft. The TOR gives more detailed motivation for wanting CFD predictions of high quality for aircraft prior to flight, including risk reduction and improved insight into characteristics. In addition, there is a requirement to analyze unanticipated events which occur in flight, and this will lead to improvements in flight-testing. Therefore one key item for the designer is to have available CFD codes and practices in which he has high confidence.

Flight data for CFD code validation has been obtained on the surface of the F-16XL-I aircraft at subsonic and transonic speeds as documented by Lamar.[2] This data is unique both in that it is for a high-performance fighter aircraft and it is publicly accessible. Furthermore, the data is not subject to wind-tunnel blockage, scaling or Reynolds-number effects. Comparison of computed and experimental data at flight Reynolds numbers, as opposed to wind-tunnel Reynolds numbers, circumvents the problem of modeling transition. Ten participants have contributed solutions to the test cases of the CAWAPI (Cranked Arrow Wing Aerodynamics Project International)'facet' of TO-AVT-113. The aim is to develop and document the best practices for each code so as to raise its technology-readiness level when applied to this class of aircraft. The flight conditions (FC) of the test cases to be examined are listed in Table 1. They represent different Reynolds/Mach number combinations at subsonic and transonic speeds, with and without side-slip.

FC	alt. [ft]	M_∞	α [°]	β [°]	Re
Minimum Flight Conditions to be examined:					
FC07	5,000	0.304	11.89	-0.133	44.40×106
FC19	10,000	0.360	11.85	+0.612	46.80×106
FC46	24,000	0.527	10.40	+0.684	46.90×106
FC70	22,300	0.970	4.37	+0.310	88.77×106
Additional Flight Conditions to be examined:					
FC25	10,000	0.242	19.84	+0.725	32.22×106
FC50	24,000	0.434	13.56	+5.310	39.41×106
FC51	24,000	0.441	12.89	-4.580	38.96×106

Table 1. Flight conditions (FC) to be studied (nominal altitude, actual Mach number, actual angle of attack, actual side-slip angle, actual Reynolds number)

Other papers presented at the two Special Sessions have discussed: the flight conditions and the test-cases,[2] the geometry of the aircraft and how the grids were generated,[3] and the ten individual codes used to obtain solutions to the test cases[4]-.[5] This paper compares cumulatively all the computed results with the flight-test measurements, makes some initial observations about these comparisons, discusses some likely causes for discrepancies, and where possible draws tentative conclusions and tries to identify lessons learned in order to take a step forward towards establishing some best practices for this class of problem.

Study Vortex Formation & Interactions Similar cumulative-comparison activities have been done before, notably among them, the series of AIAA Drag Prediction Workshops. What we do here differs in that it is a fighter configuration and the comparisons are done against flight-test data not windtunnel measurements, which makes it rather unique. Furthermore the objective is not the accurate prediction of say total drag counts, but instead is the prediction of complex vortical-flow phenomena that strongly impacts the flying qualities of a fighter aircraft because the interaction of vortices over an aircraft determines its stability and control characteristics.

Figure 1 depicts the skin-frictions lines over the F-16XL-1 aircraft and illustrates the effect that such vortical phenomena can have on the aircraft at moderate-to-high angle of attack. The airflow separates from the leading edge of the inner wing and forms a primary vortex over the surface. This vortex induces the boundary layer on the wing surface under it to separate and form a secondary vortex. Further downstream at he crank in the leading edge, these two vortices enter into a region of strong interaction with a vortex shed from the leading edge of the outer wing as well as with one shed from the airdam, all of which ultimately impact the missile at the tip. It is this nonlinear phenomena that we endeavor to simulate.

The CAWAPI test cases in Table 1 explore such phenomena in three categories of flight conditions: 1)co-

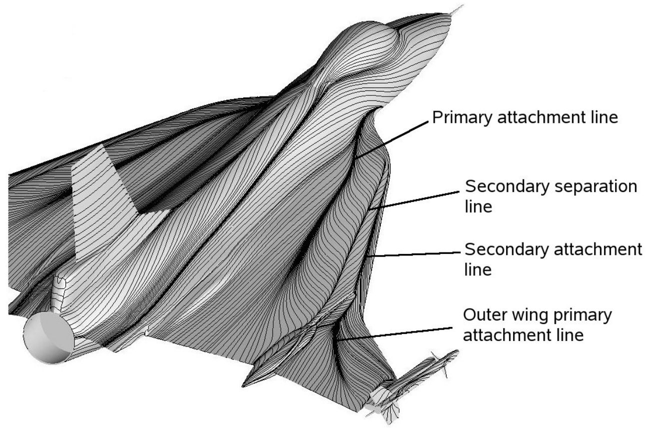

Figure 1. Example of vortex effects on the skin-friction lines of the flow over the F-16XL-1 aircraft produced by inner-wing primary and secondary vortices that interact with the outer-wing vortex at the crank, the airdam vortex and the missile at the tip (Boelens et al.[4]solution)

herent vortex flow (moderate alpha) with no significant breakdown over the wing , 2)high-alpha vortex flow with breakdown, and 3)transonic effects. Comparing the computed results with the flight-test data for these cases will show us how ell such phenomena is predicted by the ten codes.

Best Practices For a CFD code to produce an accurate solution, many *correct* choices have to be made in setting up the problem and running the code. Best practices per se are those *correct* choices, and important ones among them are:

- Geometry Definition
- Grids & Grid Design
- Numerical Accuracy

  Time accuracy, Spatial Accuracy
- Turbulence Modeling
- Boundary Conditions

After carrying out the cumulative comparisons of computed results with flight-test data, we make some initial observations of what these comparisons tell us in terms of how good were the choices with regard to: 1)grids, 2)turbulence modeling, either steady or unsteady in order to indicate which particular ones of these are the better predictor of:

- vortex formation and location
- moderate versus high angle-of-attack comparisons

  surface C_p

  Skin-friction coefficient C_f

  Flight-Re-number boundary-layer velocity profiles

  Transonic effects and shock waves

The Table of Contents, above, scopes out the structure of the sections that follow.

II. Codes Applied & Flight Conditions Simulated

Table 2 lists the ten contributors to CAWAPI: their number, used in the legend of the comparison figures, the codes they used to produce the results discussed in this paper along with relevant information about the cases solved, models employed, steady or unsteady, and grids used. The information in the table helps to understand the differences observed when comparing the cumulative results and the discussions that follow.

#	Contributor	Code/Developer	Physical Modeling ‡	Numerical Method	Str-Uns*	Cases Solved	Standard Grid	Time dep.†
1	**NLR**[4]	**ENSOLV** Version 6.20-6.32 http://www.nlr.nl/smartsite.dws?lang=en&ch=DEF&id=48	RANS TNT $k-\omega$ .2with vorticity correction	Cell-centred central difference, finite volume scheme	S	FC7, FC19, FC46, FC70, FC25, FC50, FC51	**YES** 1903 blocks, 14, 750,720 cells	Steady
2	**University of Liverpool**[6]	**PMB** ULiv	RANS Wilcox k-ω with vorticity correction	cell-centred, finite volume scheme Osher.s upwind or Roe.s flux splitting scheme	S	FC7, FC19, FC46, FC70, FC25	**YES** 21903 blocks, 14, 750,720 cells	Steady
3	**NASA/LARC**[7]	**PAB3D1** Analytical Services & Materials Eagle Aeronautics NASA Langley www.asm-usa.com/software/PAB3D/index.html	2-eq. model (k-ω), 2-eq. model SZL EASM, 2-eq. model Girimaji EASM, DES, LES, PANS, fixed transition	Cell centered, upwind Roe scheme, Implicit - 3 factor Scheme, Explicit - time accurate dual time stepping	S	-	**YES** grid 200 blocks, 14.750.720 cells, 3 level mesh sequencing	Steady
4	**KTH/FOI**[8]	**Edge**, version V3.3.1 FOI www.edge.foi.se	RANS Hellsten k-ω + EARSM model	Central second-order scheme	U	FC7, FC19, FC46, FC70, FC25, FC50, FC51	**YES** Standard NASA grid + 9 prismatic layers (generated at USAFA), 2.5M points	Steady
5	**EADS-MAS**[9]	**TAU**, actual version DLR	RANS, SAE turbulence model	Spatial discretization by AUSMDV upwind scheme, backward Euler implicit scheme in time solved with LU-SGS towards a steady state	U	FC7, FC19, FC46, FC70, FC25	**NO** solution adapted grids. Initial grid: 10M points, final adapted grids 20-22M, 30 prismatic layers	Steady

* Numerical method is a structured-grid (Str) or unstructured-grid (Uns) type method.
† Solution obtained is steady state, or unsteady with time accuracy.
‡ Turbulence models in the codes. See the specific papers for which ones are used in the computations.

Table 2. Ten contributions to CAWAPI: codes, cases solved, models used, steady or unsteady, and grids

#	Contributor	Code & Developer	Physical Modeling [‡]	Numerical Method	Str-Uns*	Cases Solved	Standard Grid	Time dep.[†]
6	**UT SimCenter**[10]	**TENASI** UT SimCenter	RANS 2eq. k-ϵ k-ω hybrid	Node-centered, finite-volume, Roe's flux-splitting, Variable Mach Preconditioning, Point implicit with sub-iterations	U	FC7, FC19, FC46, FC70, FC25, FC50, FC51	**NO** Half-model contained 14M points, 32M tetrahedra, 160K pyramids,16M prisms, 352K hexahedra	Steady
7	**NASA/LARC**[11]	**USM3D** NASA Langley Research Center http://tetruss.larc.nasa.gov/usm3d/	RANS: 1-eq. Spalart-Allmaras (SA) model, 2-eq Menter SST, 2-eq linear k-ϵ, 2-eq ARSM k-ϵ	cell centered, Roe FDS, AUSM, FVS, and HLLC, Implicit scheme, Dual time stepping, Newton method	U	FC7, FC19, FC46, FC70, FC25, FC50, FC51	**YES** Tetrahedral grid, 16161959 cells, 32323918 cells (FC50 and FC51)	Steady
8	**USAFA**[12]	**Cobalt** www.cobaltcfd.com/Codes/cobalt.htm	Hybrid RANS/LES (DES) with a modified SA 1 eq model used when in RANS mode with rotational corections - 'SARC-DES'	cell-centered, Godunov-type scheme with least square reconstruction. Implicit time stepping with Newton subiterations	U	FC7, FC19, FC46, FC70, FC25, FC50, FC51	**YES** Standard NASA grid + 9 prismatic layers, 2.5M points	Unsteady
9	**Boeing**[5]	**BCFD** (~Wind-US) Boeing www.grc.nasa.gov/WWW/winddocs	RANS Spalart-Allmaras	cell centered, Harten-Lax-van Leer (HLLE) FDS	U	FC7, FC19, FC46, FC70, FC25(Standard Grid)	**NO** manually adapted grids ~20-27 M cells for half-model	Steady
10	**LMAC**[13]	**Falcon v4 LMAC**	N/A	N/A	U	N/A	N/A	N/A

* Numerical method is a structured-grid (Str) or unstructured-grid (Uns) type method.

† Solution obtained is steady state, or unsteady with time accuracy

‡ Turbulence models in the codes. See the specific papers for which ones are used in the computations.

Table 2. Ten contributions to CAWAPI: codes, cases solved, models used, steady or unsteady, and grids

Possible Sources of Discrepancies There are a number of factors to keep in mind that can cause differences in the comparison of results. First, we are comparing flight-test measurements with results computes at *nominal* values of flight conditions, i.e. the particular flight test may have been carried out at somewhat different conditions, and there may be other uncertainties involved, such as whether a control surface was deflected or not. All computations are done at zero deflection angle, but that may not be the case for the particular flight test with which it is being compared. This is just a fact of life when working with flight testing.

When comparing one computational result against another, check if the same partial differential equations are being approximated in both results, i.e. are the equations of the physical modeling in each set the same? This pertains not only to the physics of the model in space but also in time. If the equations are not the same, then that is a source of discrepancy at the differential level. Check the numerical models next. Assuming that the differential equations being approximated are the same, what is the order of accuracy of the discrete equations that approximate the differential ones, what is its truncation error? Since all ten codes in Table 2 are formally second-order accurate in space, the relative truncation error becomes a function of the grid spacing used. And this source of discrepancy can be controlled by using a common grid for the computations. That way, if the grid is the same in two computations, the differences in results can be attributed more conclusively to the differences in physical modeling. Thus both grid resolution and physical modeling are the two prime factors that can explain observed differences in the cumulative comparisons.

Seven codes use unstructured grids, three use structured. Because of the geometric complexity of the F-16XL it is impossible to achieve grid convergence, so the only hope is to reduce truncation error locally through grid adaptation and refinement, either automatically or by manually manipulating the grid. All three structured solvers used a common mesh, providing a good basis for comparing among them. Of the seven unstructured solvers, three used standard grid without refinement or adaption, and four generated their own grids and then refined and adapted them.

A. The Standard Grids & Their Importance

Table 2 above refers to standard (or common) grids, and some explanation is necessary here.

1. *Geometry Description*

At the beginning of CAWAPI two IGES files of the F-16XL aircraft were available, one from Lockheed-Martin Aeronautics Company and one from NASA Langley. The latter was obtained by measuring the actual aircraft in the NASA hangar, where a numerical surface description (NSD) was obtained through photogrammetric targets. Using both surface descriptions and additional CATIA models for the inlet up to the compressor face and for the nozzle up to the turbine face, an updated IGES file was generated by Lockheed-Martin Aeronautics Company. It should be noted that for the configuration used the control surfaces were not deflected. This IGES file contained a better characterization of the actual aircraft surfaces and the leading edges, but was still not suitable for further grid generation purposes. It was found that the geometry description contained multiple overlaying surfaces. This was corrected at EADS-MAS, where a single set of describing surfaces was generated. The resulting description also included some refinements in the wing leading-edge region to improve future grid generation in this region. It was recognized by the CAWAPI members that this surface description needed some further adjustments to facilitate the generation of a structured grid, and these modifications

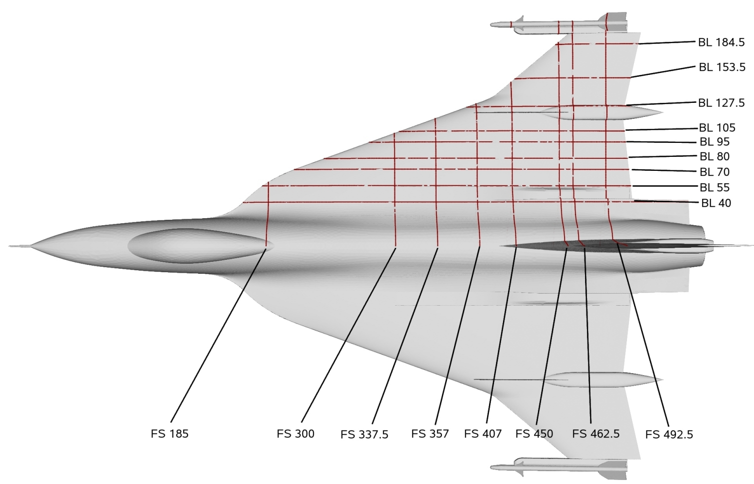

Figure 2. F-16XL-1 geometry with position of chordwise Butt Lines and spanwise Fuselage Stations along which surface C_p is measured.

were made at the NASA Langley Research Center. Finally, the modified surface description was checked for water tightness and corrected, where necessary, using the CAD-FIX tool. Figure 2 displays the water-tight geometry description used for both the structured and unstructured grid generation. It also displays the layout of the chordwise Butt Lines and the spanwise Fuselage Stations along which surface C_p is measured and compared with computations. Together these form a reasonable matrix of data points to provide insight to the formation and interaction of vortices along the wing leading edge, the crank and the airdam.

2. Grids

At the beginning of the project the working group members recognized the need to use common grids around this complex geometry to eliminate most of the uncertainties related to grid spacing, i.e. truncation error. The original plan was to have two common grids, one structured (multi-block) and one unstructured (tetrahedral). However, whereas all partners using structured CFD methods performed their simulation on a common structured multi-block grid generated at Netherlands National Aerospace Laboratory NLR (see section VI), the major of contributors using unstructured CFD methods generated during the course of the project their own unstructured grid and/or adapted some initial grid either automatically or manually.

Why Participants Generate their Own Mesh After the discussion above, it could be expected that, although all participants acknowledged the importance of a common mesh as a common base for comparing the results as well as jump starting the solution process, in the end the majority of the participants with unstructured-grid solvers would generate their own meshes. Reasons why they do this, some report is the desire to improve solution quality. This quest to improve quality is not isolated to the modification of the mesh, but includes investigation of solution-algorithm options, turbulence models, etc. If the computations are limited to a single mesh, this will eliminate the investigation of an important source of error. Another contributing reason is to reduce the uncertainty that increases when using a type of mesh that has not been validated in your flow solver. Experience from running any structured or unstructured solver over a long period of time builds up the understanding (best practices) of the mesh requirements (resolution, stretching, cell type, ...) that provide an accurate solution for that solver. Unstructured grids provide the luxury of being able to rapidly create a mesh that meets the requirements learned from hundreds of previous computations. This instills a level of comfort that the mesh is at least comparable to what has been used in the past and reduces one source of uncertainty in the computations.

III. Comparisons — Vortical Flow, no breakdown — FCs:7,19,46

This section presents primarily observations on the comparisons of computed and measured flowfield quantities for FC7, FC19 and FC46. In doing so we observe in particular the outer limits in the spread of the data, i.e. those that depart lowest and highest from the measured data.

In addition to surface C_p measurements, FC7 presents boundary-layer rake measurements. FC19 presents skin friction measured spanwise along FS300. Comparisons with this data ought to be good for distinguishing benefits of RANS-type vis-a-vis higher-order physical modeling such as DRSM or DES types. FC46 presents just C_p comparisons. Cases with sideslip, FCs 50 and 51, are not discussed in this paper.

Are there general differences between structured and unstructured code results for surface flow data? If so, what assumptions are involved that lead to the differences?

When we analyze the various comparisons of data: surface flow (C_p), boundary-layer profiles, and skin friction, we want to gain insight into:

- vortex formation and how the various vortices come into being
- influence of the airdam, actuator pod, crank
- geometry description & the effects of poor grid resolution
- effects of specific turbulence modeling, e.g. RANS and DRSM differences
- unsteady effects: do DES results differ from steady RANS ?

A. FC7: $M_\infty = 0.304$, $\alpha = 11.89°$, $Re = 44.4\ M$

Flight Condition 7 is a case of fully developed vortical flow over the upper surface with no appreciable breakdown before the trailing edge (of at least the inner-wing vortex).

1. Overall Vortical Flow Features

Figure 3 presents sectional spanwise contours of iso-total-pressure and skin-friction lines. The contour plots indicate the presence and location of the inner-wing primary and secondary vortices, the outer-wing primary and secondary vortices, and even small nose-fuselage vortices. The convergence-divergence of skin-friction lines indicate the occurrence and location of primary or secondary vortex separation-reattachment, respectively.

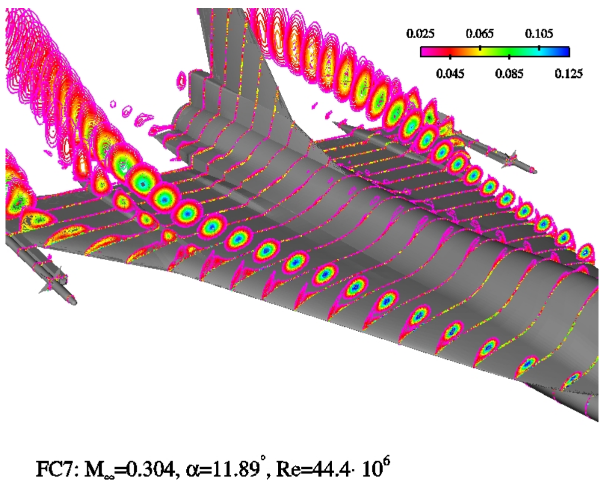

(a) **Sectional spanwise contours showing vortical flow features over upper surface**

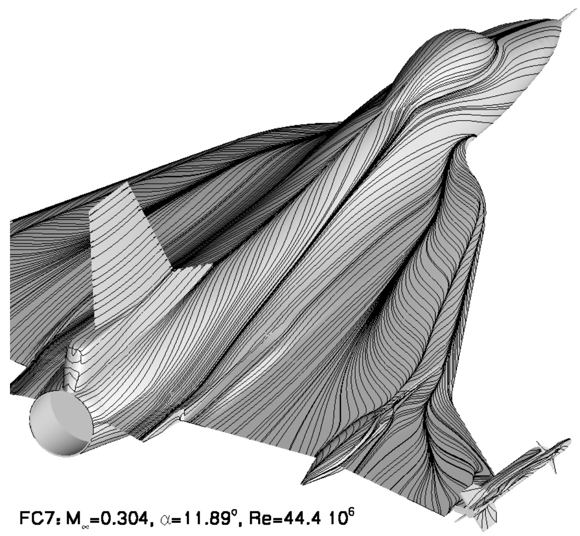

(b) **Skin friction lines on the upper surface**

Figure 3. Vortical-flow features over upper surface for FC7: inner-wing primary and secondary vortices, outer-wing primary and secondary vortices, and even small nose-fuselage vortices: a) iso-total-pressure contours, b) skin-friction lines $M_\infty = 0.304$, $\alpha = 11.89°$, $Re = 44.4\ M$, Boelens et al.[4]

2. C_p Comparisons along Butt-line Sections

Figure 4 presents comparisons of the computed and flight-tested surface pressure coefficients C_p plotted along the butt-lines. The first four of these shows good overall agreement between the computed and tested results. The inner wing vortex is being resolved, as is the outer-wing vortex. The leading edge vortex forms in the vicinity of BL55. There are differences in the suction peaks due to the vortex, and Fig 5 shows these in an expanded horizontal scale.

At BL95 in Fig 4 the pressure distribution begins to be effected by the airdam and differences begin to grow in the spread of the peak. Also the ULiv results shows another peak near 60% chord. The surface skin-friction lines computed in Fig 6 show that the airdam and actuator pod are major disturbances to the upper surface flow. At BL153.5 some computed peaks are inboard of the flight-test peak while are computed peaks are much lower. At BL184.5 some computed results show a peak while others do not, and nor do the test results. These differences presumably are brought on by the effects of the airdam.

Detail comparison of C_p values zoomed on first 30% of chord Figure 5 examines the peaks along the first 30% of the chord for four butt-lines. At BL55 the EADS-MAS results are highest and also show a secondary vortex suction peak. This could be the effect of the vortex-correction terms in the turbulence model. The UTSimC peak is the lowest. The extent of the disparity shown here indicates the effects of grid spacing and turbulence modeling in the vicinity of the inner-wing vortex formation. At BL70 the NLR peak

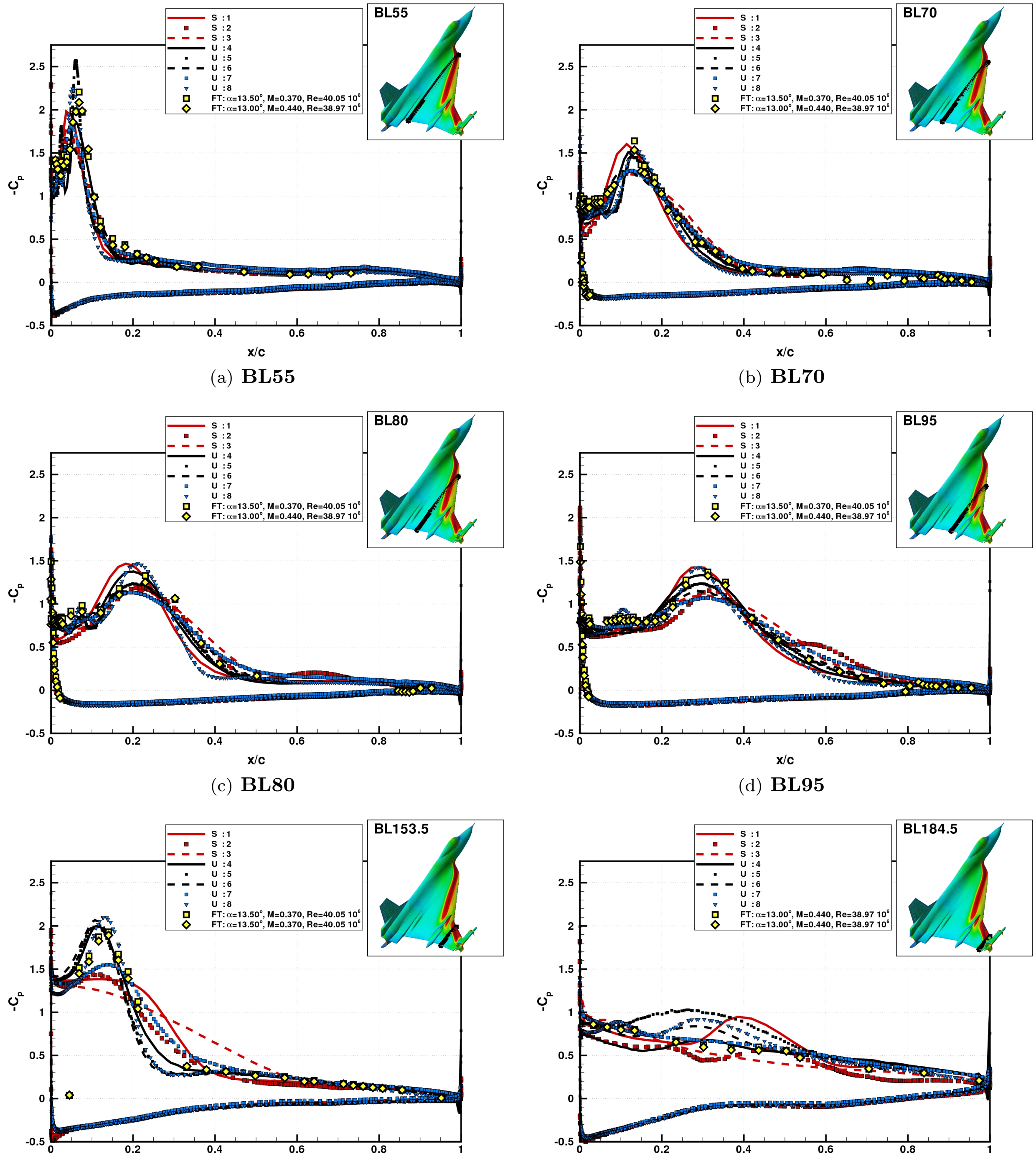

(a) **BL55** (b) **BL70**

(c) **BL80** (d) **BL95**

(e) **BL153.5** (f) **BL184.5**

1 - NLR, 2 - ULiv, 3 - NASA-S, 4 - KTH/FOI, 5 - EADS-MAS,
6 - UTSimC, 7 - NASA-U, 8 - USAFA, 9 - Boeing, 10 - LMAC

Figure 4. Chordwise comparison of computed and measured surface pressure coefficient along six butt-lines (BL) for case FC7: a) BL55, b) BL70, c) BL80, d) BL95, e) BL153.5, f) BL184.5

is slightly upstream of the others, and this trend continues in BL80. At BL153.5 more computed peaks are shifted slightly upstream of the test peak of the outer-wing vortex, less so for the USAFA results. Others show hardly any peak, e.g. the NASA-S results. But keep in mind that the flight test was done at 1° higher alpha.

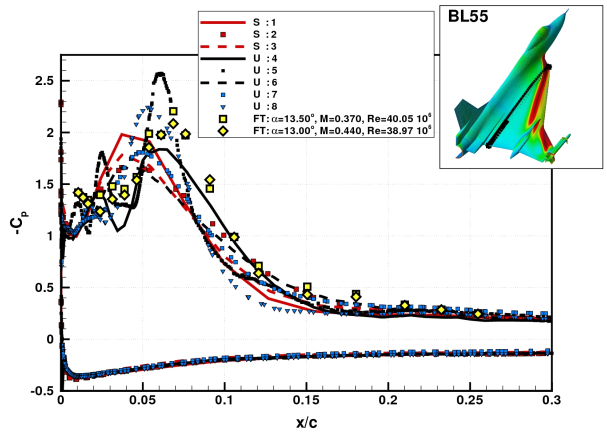

(a) **BL55**

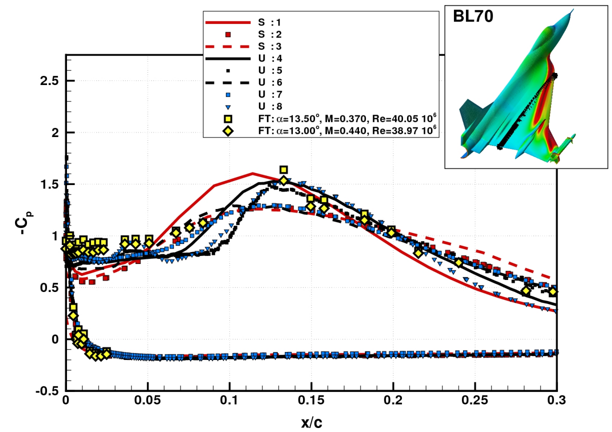

(b) **BL70**

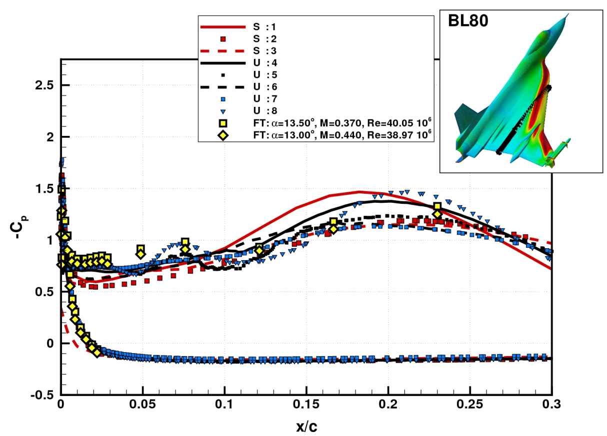

(c) **BL80**

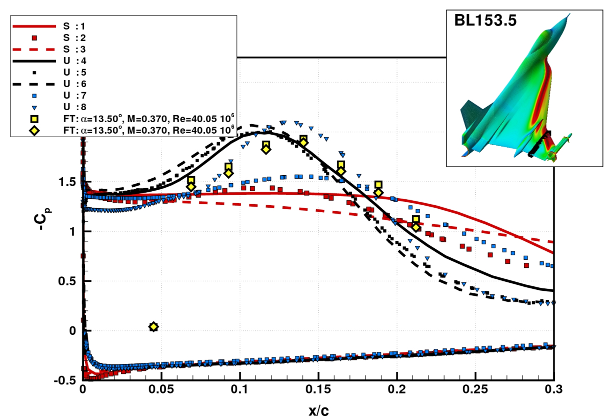

(d) **BL153.5**

1 - NLR, 2 - ULiv, 3 - NASA-S, 4 - KTH/FOI, 5 - EADS-MAS,
6 - UTSimC, 7 - NASA-U, 8 - USAFA, 9 - Boeing, 10 - LMAC

Figure 5. FC7 Expanded view of surface C_p along BL cuts over first 30% chord

3. C_p Comparisons along Fuselage Stations

Let us now examine spanwise plots of C_p in Fig 7. At FS300 there is a spread in the peak values at 80% span, and the USAFA results show a strong secondary vortex peak. Other results indicate no secondary vortex. We may expect effects here from the turbulence models. We see a blip in the pressure values of the KTH/FOI and EADS-MAS results at about 50% span. This is due to a flaw in the geometry definition, as shown by Fig 8.

At FS337.5 this blip is gone. Some solutions start to pick up the secondary vortex peaks. At FS375 the main feature is the effect of the airdam at 94% span. The computed results show differing variations in the spanwise pressure around the airdam. Compare this with the surface flow in Fig 6.

At FS407.5 there are substantial differences in results for the airdam vortex peak and outer-wing vortex at the outboard 20% span, presumably due to variations in grid resolution here. At FS450 there are major differences in results for the outer-wing vortex peak and the flow overthe actuator pod near 60% span.

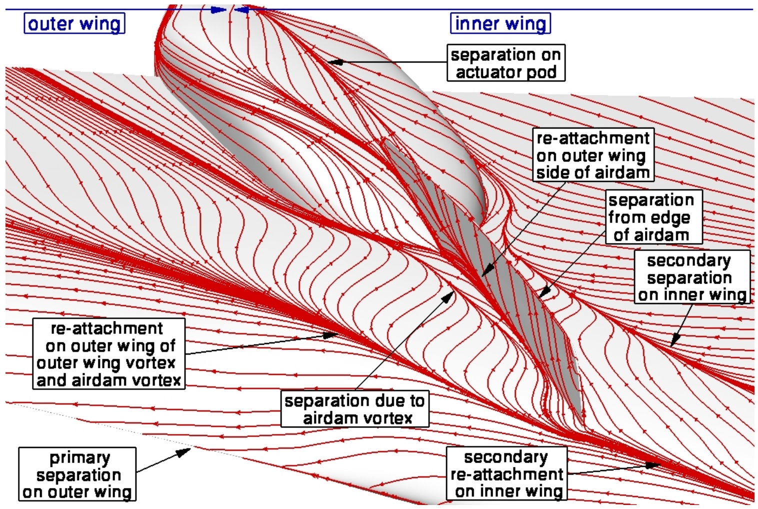

Figure 6. Surface skin-friction lines over airdam/actuator-pod in the outer-wing interaction zone, FC7, Boelens et al.[4]

4. Comparisons of Velocity Profiles in Boundary Layer

Figure 9 presents comparisons of the computed and measured velocity profiles in the upper-surface boundary layer of FC7 at four locations plotted in the vertical direction z over the wing. In all locations the computed results are banded around the measured values. At Rake3, located inboard of the primary attachment line, i.e. mainly streamwise flow, the NLR and EADS-MAS results are the most full profiles, indicating a higher turbulence level than what is measured. The NASA-U results are the most deficit results, indicating a too low level of turbulence.

At Rake4, located nearly under the primary vortex, the band is tighter with the USAFA results most deficit and the NASA-U results fullest. At Rake5, located approximately under the secondary vortex, the USAFA results are now fullest and the ULiv results most deficit. At Rake7, located slightly outboard of Rake5, the USAFA results are so full as to be unrealistic, and the EADS-MAS is most deficit.

In order to compare these results better, Fig 10 plots the computed and measured velocity profiles on a logarithmic scale of the vertical distance z over the upper surface. This gives a better view of the slope of the profile at the wall. The measured results do not go much below 1mm. At Rake3, above 1mm, the KTH/FOI and EADS-MAS results are too full, but below 1mm these appear to re-join the trend of the other computed results.

At Rake4 the NLR results are too full above 1mm and re-join the trend of the other computed results smoothly below 1mm. At Rake5 it is USAFA results that are too full above 1mm. Below 1mm the spread in the band of computed results is larger than at the previous two rake stations. At Rake7, apart from the USAFA results, those of NLR are next most full above 1mm. Below that level the spread in the band is less than in Rake5.

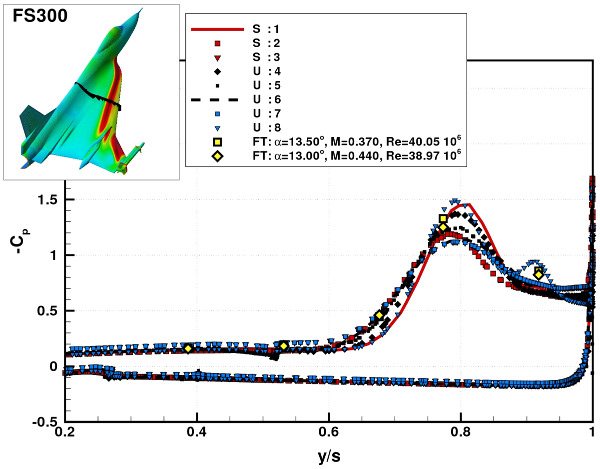

(a) **FS300**

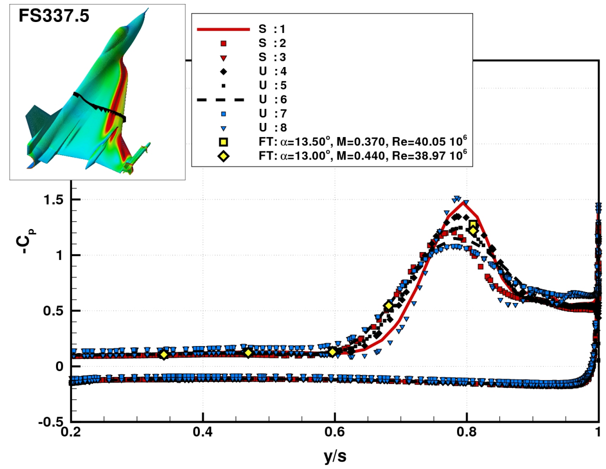

(b) **FS337.5**

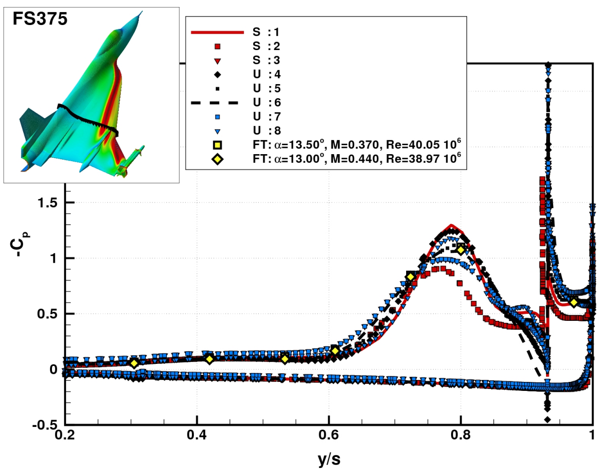

(c) **FS375**

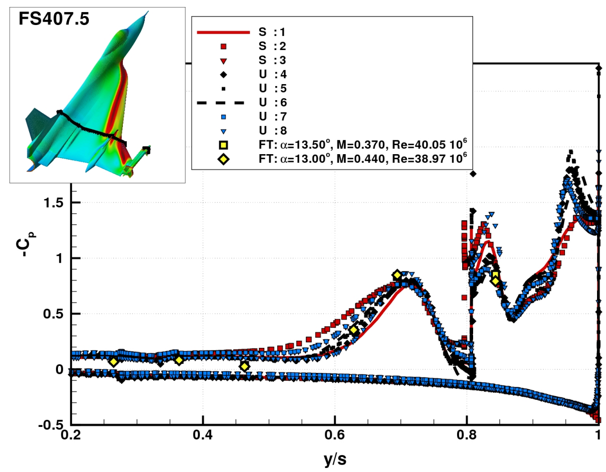

(d) **FS407.5**

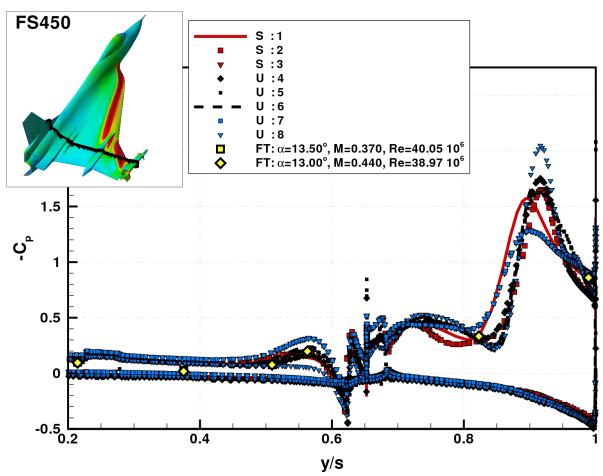

(e) **FS450**

1 - NLR	2 - ULiv,	3 - NASA-S,	4 - KTH/FOI,	5 - EADS-MAS,
6 - UTSimC,	7 - NASA-U,	8 - USAFA,	9 - Boeing,	10 - LMAC

Figure 7. Spanwise comparison of computed and measured surface pressure coefficient along five fuselage-station lines (FS) for case FC7: a) FS300, b) FS337.5, c) FS375, d) FS407.5, e) FS450

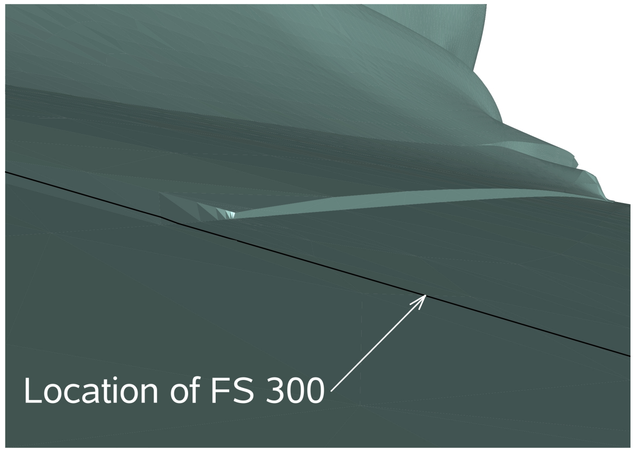

Figure 8. Kink in geometry, black line shows position of FS300 station

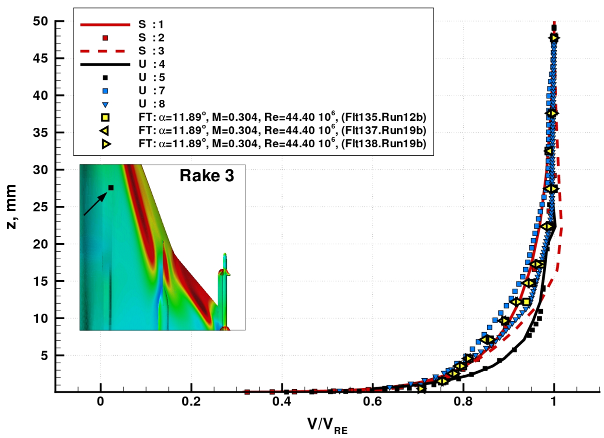

(a) **Rake3**

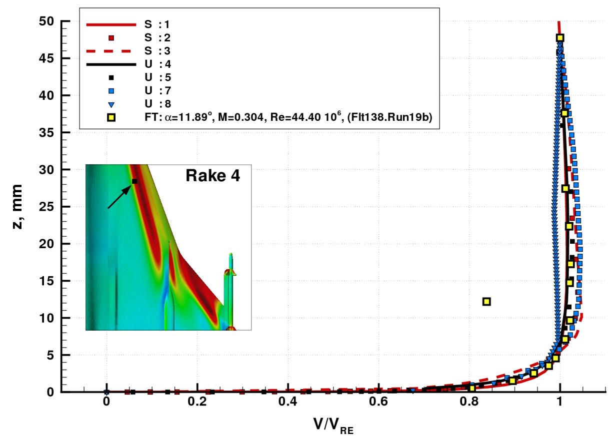

(b) **Rake4**

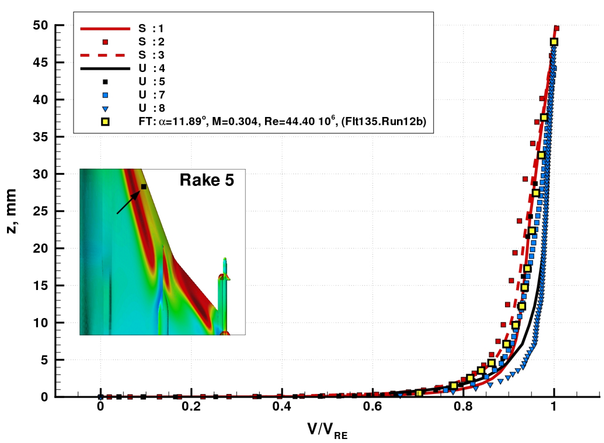

(c) **Rake5**

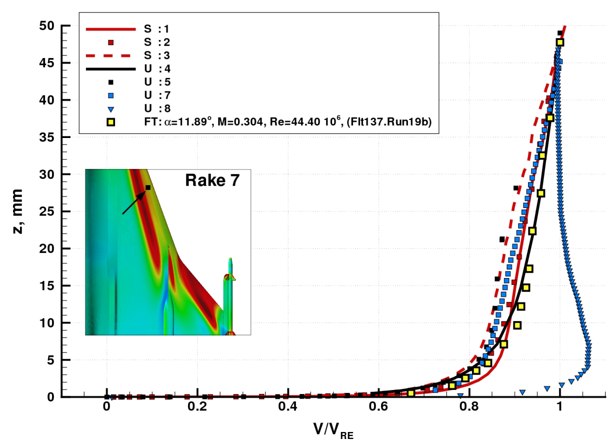

(d) **Rake7**

1 - NLR	2 - ULiv,	3 - NASA-S,	4 - KTH/FOI,	5 - EADS-MAS,
6 - UTSimC,	7 - NASA-U,	8 - USAFA,	9 - Boeing,	10 - LMAC

Figure 9. Comparisons of computed and measured velocity profiles in the upper-surface boundary layer of FC7 at four locations: a) Rake3, b) Rake4, c) Rake5, d)Rake7

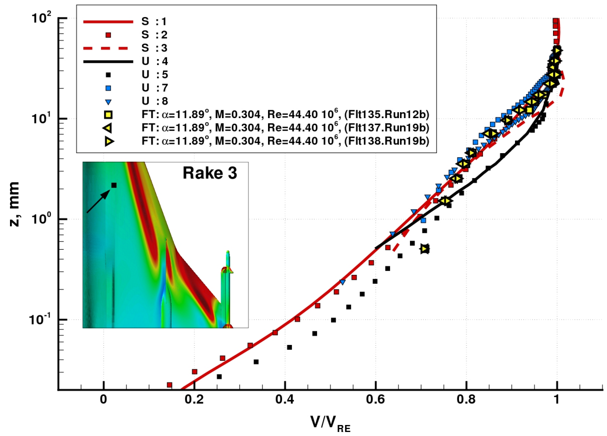

(a) **Rake3**

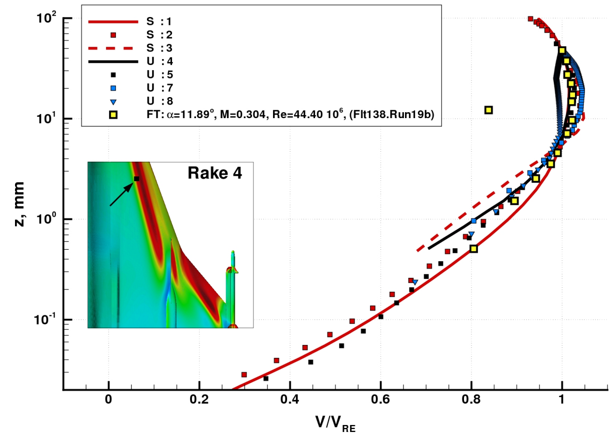

(b) **Rake4**

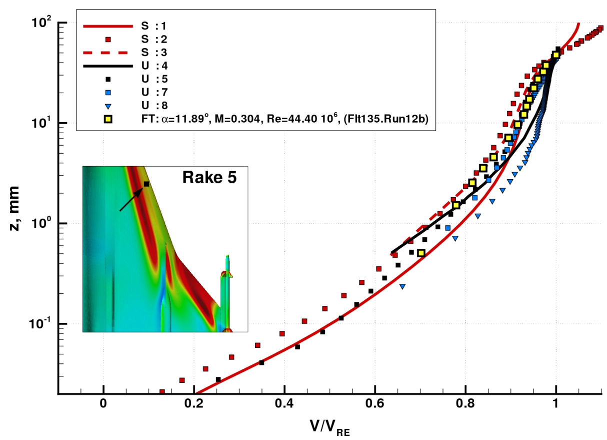

(c) **Rake5**

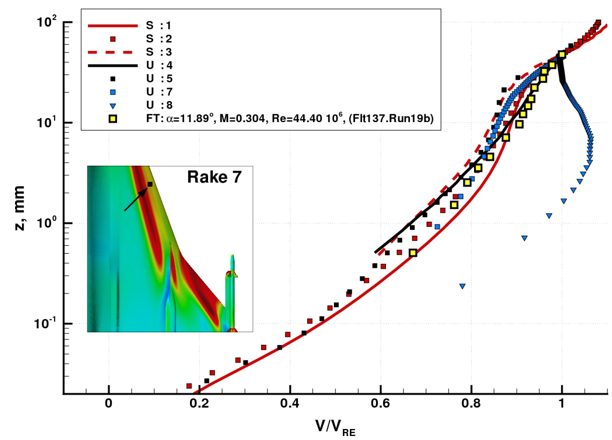

(d) **Rake7**

1 - NLR	2 - ULiv,	3 - NASA-S,	4 - KTH/FOI,	5 - EADS-MAS,
6 - UTSimC,	7 - NASA-U,	8 - USAFA,	9 - Boeing,	10 - LMAC

Figure 10. Comparisons of computed and measured velocity profiles in the upper-surface boundary layer of FC7 plotted on a logarithmic scale of vertical distance z at four locations: a) Rake3, b) Rake4, c) Rake5, d)Rake7

B. FC19: $M_\infty = 0.36$, $\alpha = 11.85°$, $Re = 46.8$ M

Flight Condition 19 is also a case of fully developed vortical flow over the upper surface with no appreciable breakdown before the trailing edge (of at least the inner-wing vortex). A close comparison of Figs 3 and 11 substantiates that these conditions are close enough to FC7 to allow cross comparisons and interpretations between the two sets of data.

1. *Overall Vortical Flow Features*

Figure 11 presents sectional spanwise contours of iso-total-pressure and skin-friction lines. The contour plots indicate the presence and location of the inner-wing primary and secondary vortices, the outer-wing primary and secondary vortices, and even small nose-fuselage vortices. The convergence-divergence of skin-friction lines indicate the occurrence and location of primary or secondary vortex separation-reattachment, respectively.

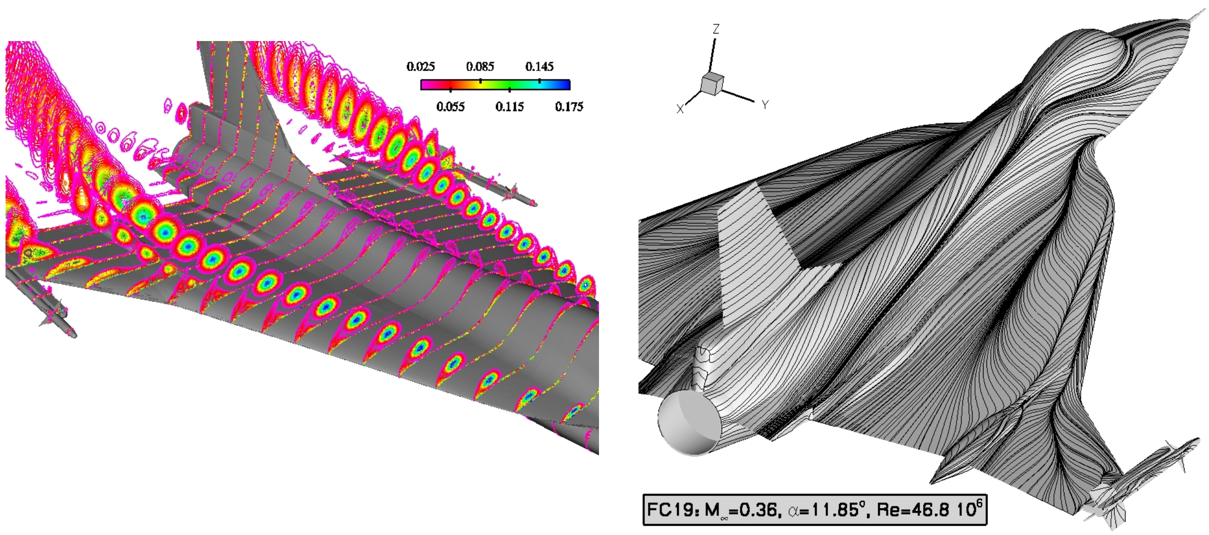

(a) **Sectional spanwise contours showing vortical flow features over upper surface**

(b) **Skin friction lines over upper surface**

Figure 11. Vortical-flow features over upper surface for FC19: inner-wing primary and secondary vortices, outer-wing primary and secondary vortices, and even small nose-fuselage vortices: a) iso-total-pressure contours, b) skin-friction lines, Boelens et al.[4]

2. *Comparison of skin-friction coefficient at FS330*

Figure 12 compares spanwise at FS330 the computed and measured values of the magnitude of the skin-friction coefficient $\mathbf{C}_f$, a vector quantity. The location FS330 is in the general vicinity of the boundary-layer rakes discussed in Figs 9 and 10. We see however a much greater spread in computed values of C_f compared with the measured ones, than we saw in the boundary-layer profiles. The measured values show two peaks in C_f, the highest under the primary inner-wing vortex and the lower one under the secondary inner-wing vortex. The computed results of NASA-U shows three peaks, the inboard one occurs at a location where there are no measurements that could confirm it. This peak may be caused by the geometry flaw. The other two computed peaks have values over the measured values. The KTH/FOI results also indicate three peaks, but its values are under the primary peak and near to the secondary peak. The USAFA results are lowest of the computed values but near to the measured secondary peak.

We must keep in mind that there are several ways to extract C_f from a computed flowfield solution. Some of the contributors plot values of C_f determined from the same expression for computing the stress tensor τ that is used in the code for obtaining the solution. Others have used a separate expression that is finite-differenced to give the resulting values. The numerical values thus obtained from these various methods may be different, but we expect the differences to be slight and not the cause of the spread of data in Fig 12.

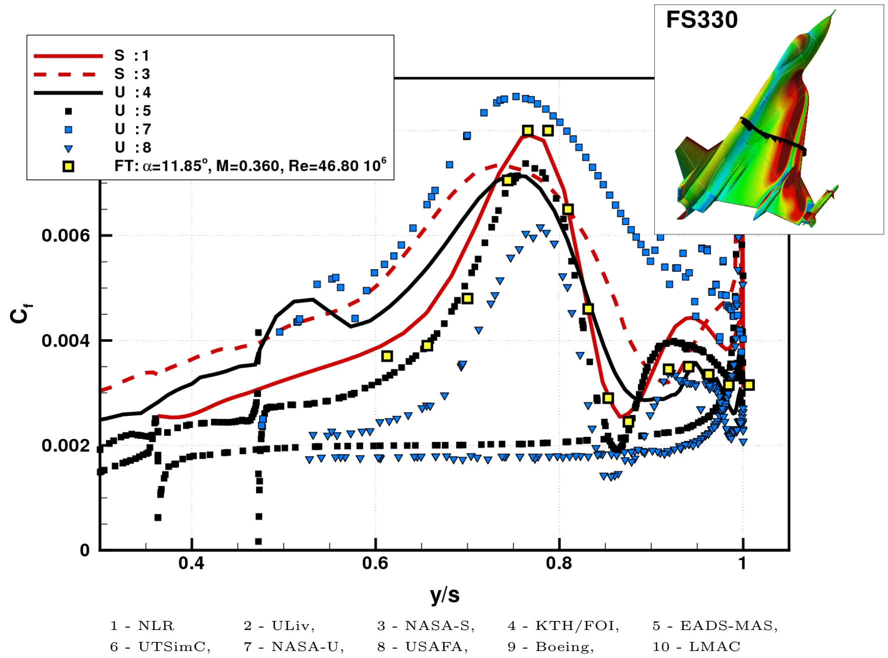

Figure 12. Spanwise comparison of the computed and measured values of the magnitude of the skin-friction coefficient C_f at FS330 for FC19

C. FC46: $M_\infty = 0.527$, $\alpha = 10.4°$, $Re = 46.9\ M$

Flight Condition 46 is also a case of fully developed vortical flow over the upper surface with no appreciable breakdown before the trailing edge (of at least the inner-wing vortex). A close comparison of Figs 3, 11 and 13 substantiates that all three conditions are close enough to each other to allow cross comparisons and interpretations between the three sets of data.

1. Overall Vortical Flow Features

Figure 13 presents sectional spanwise contours of iso-total-pressure and skin-friction lines. The contour plots indicate the presence and location of the inner-wing primary and secondary vortices, the outer-wing primary and secondary vortices, and even small nose-fuselage vortices. The convergence-divergence of skin-friction lines indicate the occurrence and location of primary or secondary vortex separation-reattachment, respectively. The EADS-MAS results pick up the geometry flaw just before 50% span.

2. C_p Comparisons along Butt-line Sections

Similar to above when discussing FC7, Figure 14 presents comparisons of the computed and flight-tested surface pressure coefficients C_p plotted along the butt-lines. The first two of these (BL55 and BL70) show good overall agreement between the computed and tested results. The inner-wing vortex is being resolved. The leading edge vortex forms in the vicinity of BL55. There are differences in the suction peaks due to the vortex. No separate zoom plot is presented for this case, but there is sufficient resolution in the electronic version of this paper to allow zooming in on the peak to see the differences. Doing so reveals less spread in the data than that seen in Fig 5.

At BL80 and BL95 the spread in data at the peak grows, with most computed values higher than the measured ones, and some computed peaks are shifted slightly upstream compared to the measured values. The NASA-S results under-predicts the suction peak. Most computed data indicate a secondary-vortex-type peak that is higher than the one seen in the measurements.

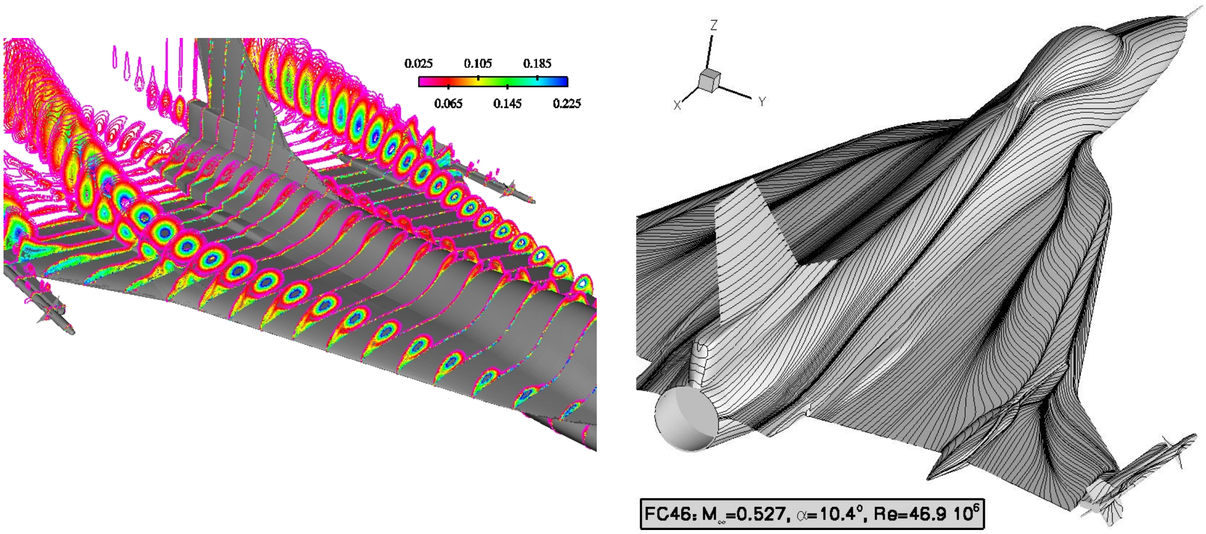

(a) **Sectional spanwise contours showing vortical flow features over upper surface**

(b) **Skin friction lines over upper surface**

Figure 13. Vortical-flow features over upper surface for FC46: inner-wing primary and secondary vortices, outer-wing primary and secondary vortices, and even small nose-fuselage vortices: a) iso-total-pressure contours, b) skin-friction lines, Boelens et al.[4]

The chordwise lines at BL153.5 and BL184.5 are located outboard of the airdam/actuator-pod. The results show a wide disparity in pressure distributions. At BL153.5 the computed peaks (under the outer-wing vortex) all appear to be downstream of the measured peak, with the USAFA values being higher than the measurements and the NASA-S values being lowest below the measurements and do not indicate any peak. At BL184.5 there is no peak in the measured data, and none in the computed results except for the NLR, ULiv, KTH/FOI and USAFA results. The lack of this peak may suggest that the primary outer-wing vortex has broken down, perhaps under disturbance from the shear layers separating from the airdam/actuator-pod (see for example Fig 6).

At BL95 begins to be effected by the airdam and Also the ULiv results shows another peak near 0.6 chord. The surface skin-friction lines computed in Fig 6 show that the airdam and actuator pod are major disturbances to the upper surface flow. At BL153.5 some computed peaks are inboard of the flight-test peak while are computed peaks are much lower. At BL184.5 some computed results show a peak while others do not, and nor do the test results. These differences presumably are brought on by the effects of the airdam.

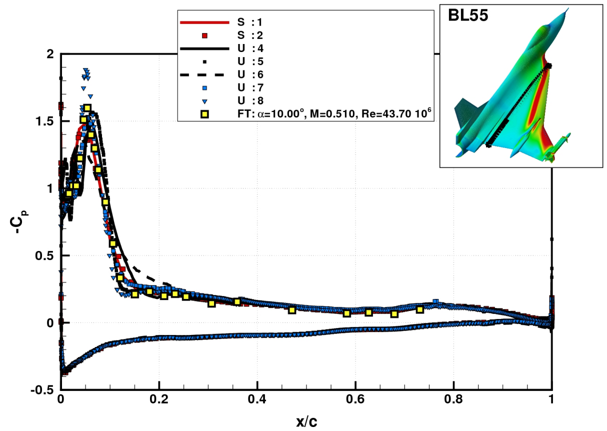

(a) **BL55**

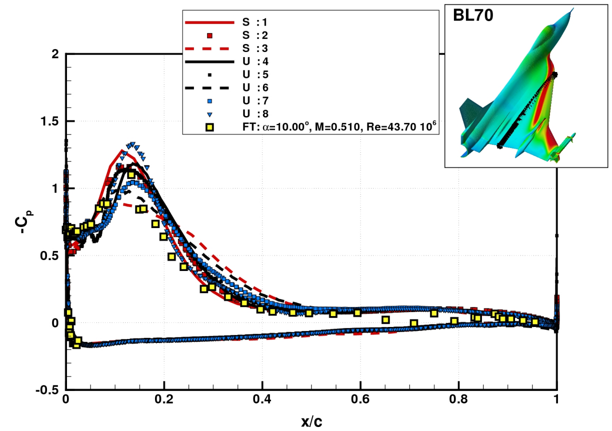

(b) **BL70**

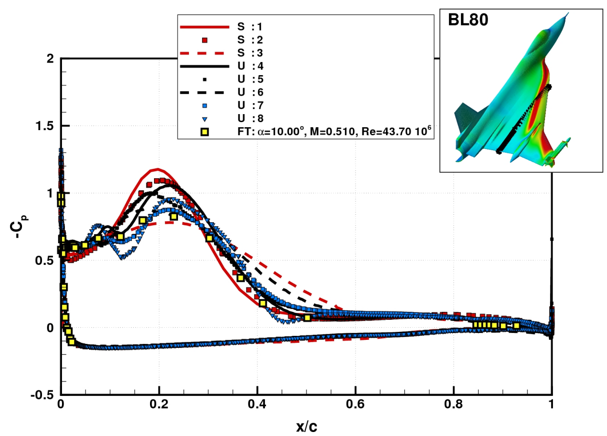

(c) **BL80**

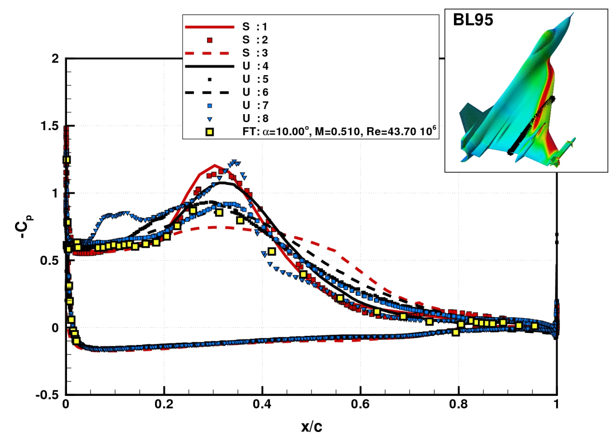

(d) **BL95**

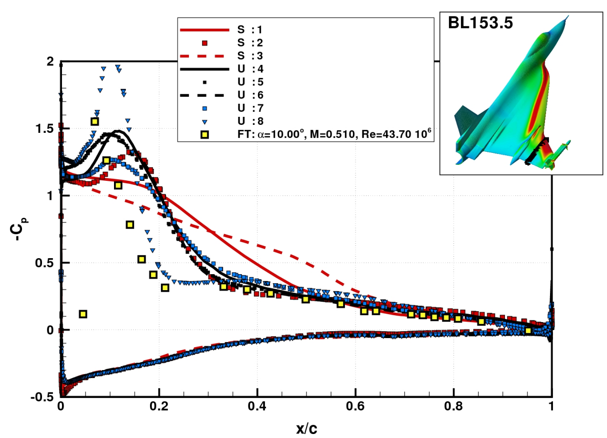

(e) **BL153.5**

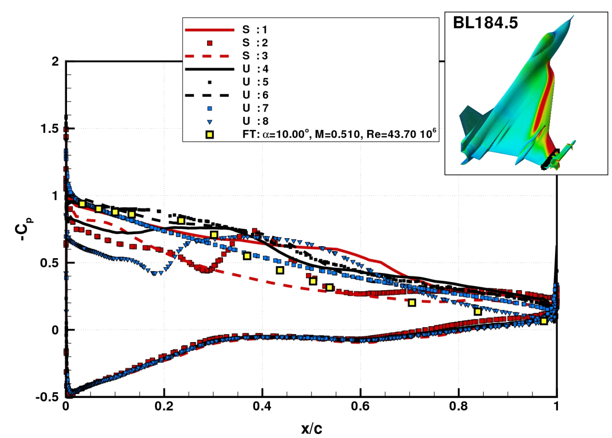

(f) **BL184.5**

1 - NLR, 2 - ULiv, 3 - NASA-S, 4 - KTH/FOI, 5 - EADS-MAS,
6 - UTSimC, 7 - NASA-U, 8 - USAFA, 9 - Boeing, 10 - LMAC

Figure 14. Chordwise comparison of computed and measured surface pressure coefficient along six butt-lines (BL) for case FC46: a) BL55, b) BL70, c) BL80, d) BL95, e) BL153.5, f) BL184.5

IV. Comparisons — Vortex Breakdown at High α — FC25

$M_\infty = 0.242$, $\alpha = 19.8°$, $Re = 32.22\ M$

Flight Condition 25 has an angle of attack nearly twice as large as the previous cases, FC7, FC19 and FC46, so we must expect stronger vortical-flow phenomena over the upper surface, perhaps even vortex breakdown over the aircraft. Unsteady flow is also associated with such phenomena and hence this may be a good case to gauge the differences between the physical modeling of steady RANS and DES, compared with flight tests.

A. Overall Vortical Flow Features

Figure 15 presents sectional spanwise contours of iso-total-pressure and skin-friction lines. The contour plots indicate the presence and location of the inner-wing primary and secondary vortices, the outer-wing primary and secondary vortices, but those small nose-fuselage vortices that we saw in Figs 3, 11 and 13 are not present. The convergence-divergence of skin-friction lines indicate the occurrence and location of primary or secondary vortex separation-reattachment, respectively. Figure 15b suggests that the separation layer on the fuselage is now drawn outboard towards the actuator pod where it may merge with the vortical flow around that structure.

Comparing the contour plots of the inner-wing and outer-wing vortices over the aft portion of the aircraft with those in Figs 3, 11 and 13 may suggest that these vortices have broken down. This is just a conjecture and remains an open question. A simple 70° swept delta wing usually does not undergo vortex breakdown at $\alpha = 20°$ in a windtunnel. But here the situation is more complex. The F-16XL has two sweep angles, 70° for the inner wing and 50° for the outer wing. Increasing leading-edge sweep decreases the leading-edge vortex strength and delays vortex breakdown so we ought not expect breakdown over the outer wing. But there is strong interaction in this double-delta vortex system over the F-16XL, further complicated by the varying leading-edge radius from root to tip. So predictions are difficult, for example the strake vortex of the F-18 experiences breakdown at $\alpha = 20°$ angle of attack. What happens over the outer wing, and in particular in the interaction zone around the airdam/actuator-pod/crank is of primary interest for the comparison of results. The isobars colored over the upper surface and inset in Fig 16a illustrates the general character of this interaction. We see here the inner-wing secondary vortex striking the airdam and then an airdam vortex issuing downstream. We also see the outer-wing primary vortex forming at the crank and traveling downstream and outboard towards the tip with its missile store.

Lastly, the answer to whether the vortex breaks down depends on how we define vortex breakdown. Is it when the axial component of velocity in the core becomes zero or turns negative, or is it simply when the vortex core becomes less coherent (in some sense)? Such issues must be kept in mind as we observe the comparisons of results that follow here.

B. C_p Comparisons along Butt-line Sections

Similar to the previous three flight conditions, Figure 16 presents comparisons of the computed and flight-tested surface pressure coefficients C_p plotted along the butt-lines, the first four along the inner wing and the last two along the outer wing where we expect strong interactions.

The first two butt-lines,(BL55 and BL70) show that the inner-wing vortex is being resolved. The leading edge vortex forms in the vicinity of BL55. The measured values show a primary-vortex peak as well as a secondary-vortex peak, as do some, but not all, of the computed results. At BL55 the NASA-U results show lowest values for the primary peak and contain a curious blip just before 40% chord. The highest values for the peak are found in the results of USAFA and NASA-S. The spread in the peak data becomes larger in BL70 where now the KTH/FOI results are the highest over the measured ones. The curious drop in two measured values near the 60% chord are due to a flap deflection during flight testing and caused by a gap in the flap or a leaking flap seal. The suction peak in BL80 is lower than in the previous two cuts, with a similar spread in computed results, some with a secondary-vortex peak and others without. The measurements show a secondary-vortex peak. And the same remarks pertain to BL95 where here the suction peak is even lower, presumably due to the beginning influence of the crank/airdam/actuator-pod.

Lines BL153.5 and BL184.5 are located outboard of the airdam-crank and those effects are felt. At BL153.5 the computed results as well as the measured ones indicate the suction peak from the outer-wing primary vortex and a smaller peak near 75% chord from the airdam vortex, with substantial spread in

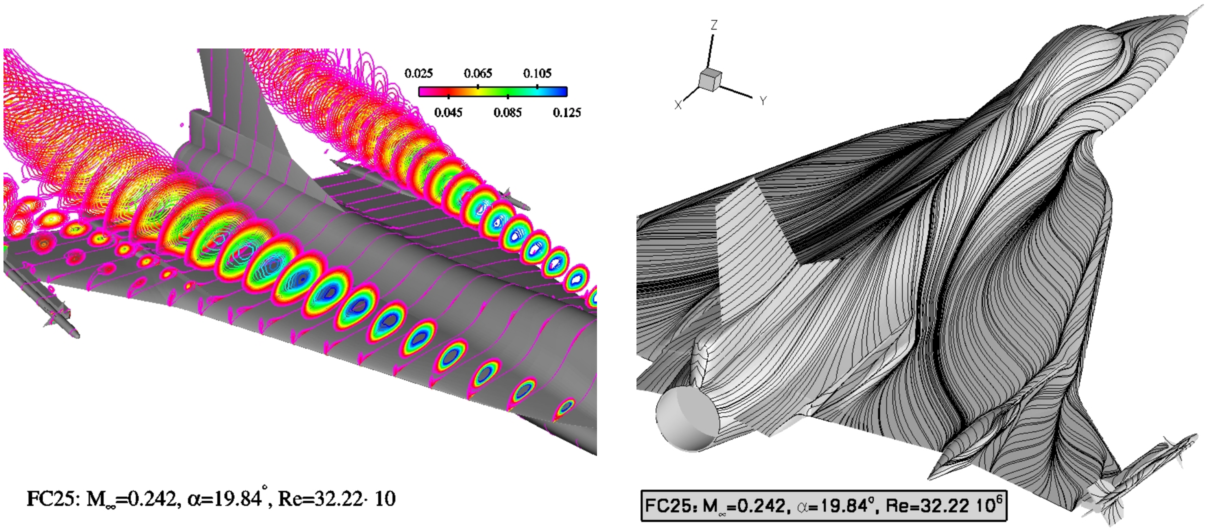

(a) **Sectional spanwise contours showing vortical flow features over upper surface**

(b) **Skin-friction lines over upper surface**

Figure 15. Vortical-flow features over upper surface for FC25: inner-wing primary and secondary vortices, and outer-wing primary and secondary vortices: broken down? a) iso-total-pressure contours, b) skin-friction lines, Boelens et al.[4]

the computed data at these peaks. At BL184.5 the outer-wing primary-vortex peak is much reduced in the measurements, with a pressure plateau that follows it further down chord, due presumably to blocking effects of the missile. The spread in the computed results is greatest for this pressure plateau, with the UTsinC results showing a suction peak.

C. C_p Comparisons along Fuselage Stations

We next examine spanwise plots of C_p in Fig 17. At FS300 the measured data show the inner-wing primary vortex peak, but not the secondary peak because there are too few measurements here. A inner-wing secondary vortex peak is expected however, and one appears in the USAFA and EADS-MAS results just past 90% span. There is a spread in the computed data for the primary vortex peak centered just before 80% span. Similar remarks apply at FS337.5 where the secondary vortex is weaker and only picked up in the USAFA results. The curious blip in the NASA-U results near 45% span may be due to the geometry flaw.

The next three stations capture the interactions of the airdam, the crank, the actuator pod and the missile. At FS375 the computed results for the primary-vortex peak is banded on the measured values. Further outboard (where there are no measured data points) the computed pressure distributions differs among each other up to the airdam at 93% span, and less so outboard of the airdam where there is just one measured data point. Spanwise along the FS407.5 station there are three suction peaks: the inner-wing primary-vortex at about 67% span, the airdam vortex at about 85% span and the outer-wing primary vortex at about 95% span. Only three computed results are plotted (for reasons unknown) and they show reasonable agreement with the few measured data points. The full set of computed results are plotted for FS450 and show large variation in the pressure over the actuator pod (60% span), the airdam-vortex peak (73% span) and the outer-wing primary-vortex peak (90% span). The only two measured data points are in the troughs of these peaks, within the band of computed data. There is also a curious blip near 25% due to a geometry feature.

V. Comparisons — Transonic Effects, Low α — FC70

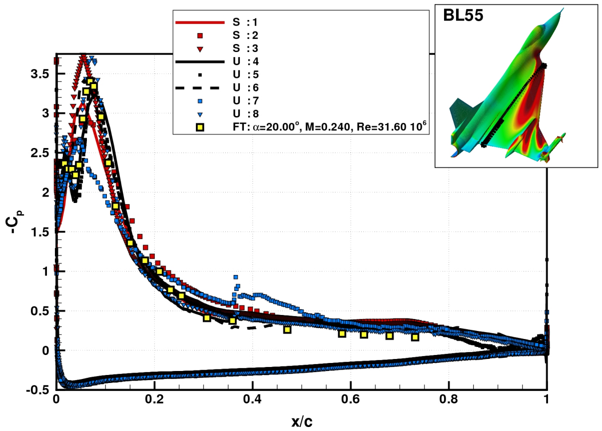

(a) **BL55**

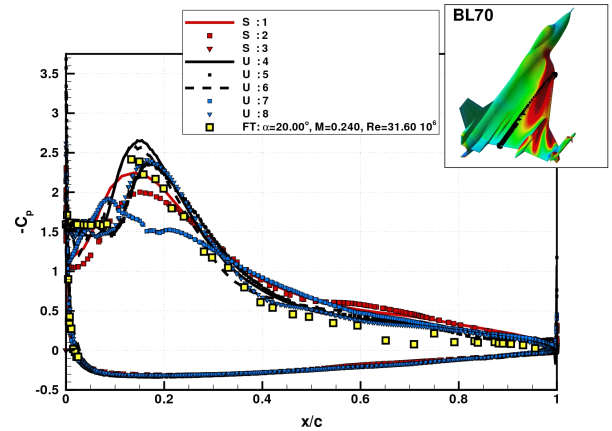

(b) **BL70**

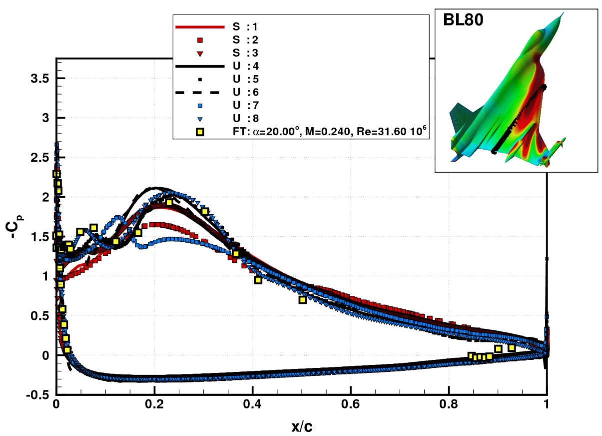

(c) **BL80**

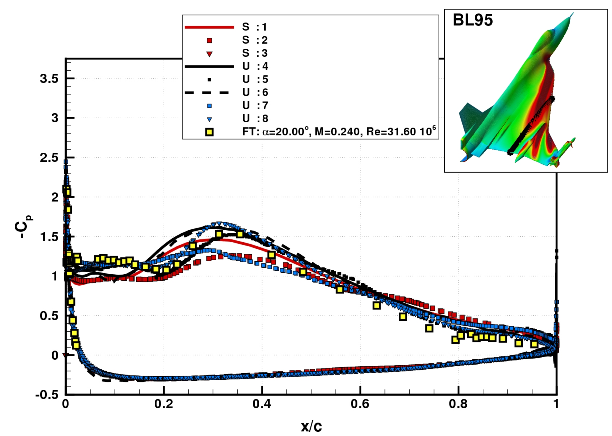

(d) **BL95**

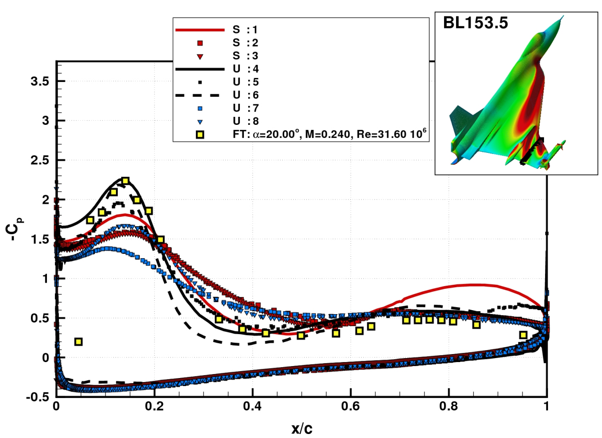

(e) **BL153.5**

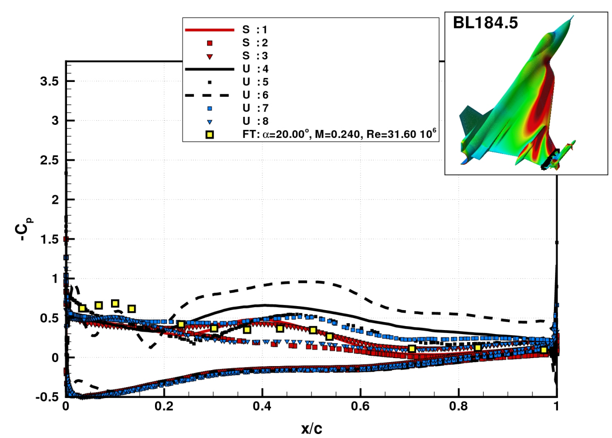

(f) **BL184.5**

1 - NLR	2 - ULiv,	3 - NASA-S,	4 - KTH/FOI,	5 - EADS-MAS,
6 - UTSimC,	7 - NASA-U,	8 - USAFA,	9 - Boeing,	10 - LMAC

Figure 16. Chordwise comparison of computed and measured surface pressure coefficient along six butt-lines (BL) for case FC25: a) BL55, b) BL70, c) BL80, d) BL95, e) BL153.5, f) BL184.5

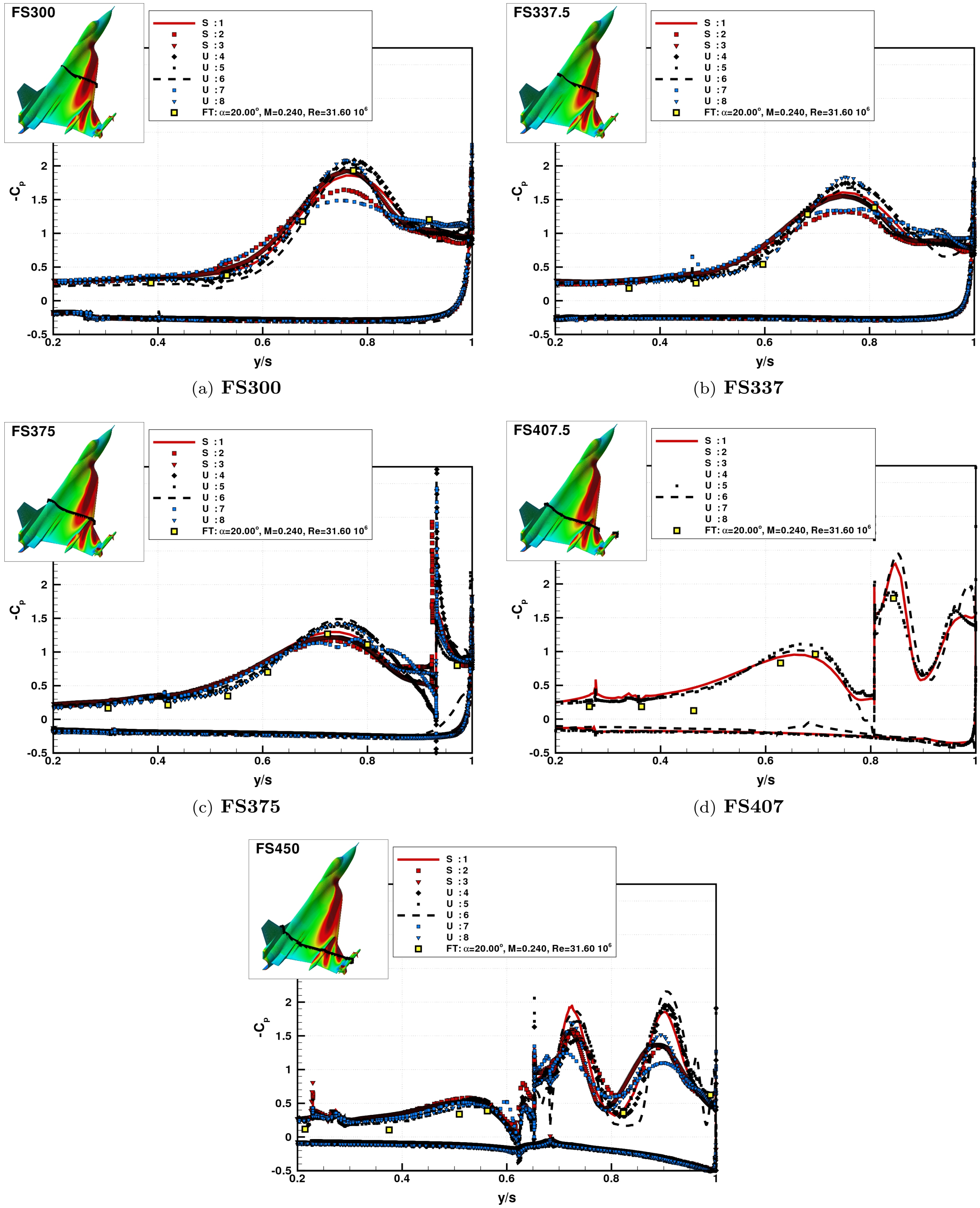

(a) **FS300** (b) **FS337**

(c) **FS375** (d) **FS407**

(e) **FS450**

1 - NLR, 2 - ULiv, 3 - NASA-S, 4 - KTH/FOI, 5 - EADS-MAS,
6 - UTSimC, 7 - NASA-U, 8 - USAFA, 9 - Boeing, 10 - LMAC

Figure 17. Spanwise comparison of computed and measured surface pressure coefficient along five fuselage-station lines (FS) for case FC25: a) BL55, b) BL70, c) BL80, d) BL95, e) BL153.5, f) BL184.5

$$M_\infty = 0.97,\ \alpha = 4.3°,\ Re = 88.8\ M$$

Flight Condition 70 has an angle of attack less than half of the previous cases, FC7, FC19 and FC46, and from two to nearly three times the Mach number, so we should expect little vortical-flow phenomena over the upper surface and strong transonic effects, i.e. shock waves. Keep in mind there is some degree of uncertainty in the flight-test data concerning whether, and how much, a flap was deflected during the measurements. Transonic effects are also very sensitive to flight conditions. The nominal conditions for the computations are $M_\infty = 0.97$, $\alpha = 4.3°$, and $M_\infty = 0.95$, $\alpha = 3.6°$ for the flight tests.

A. Overall Vortical Flow Features of FC70

Figure 18 presents sectional spanwise contours of iso-total-pressure and skin-friction lines. The contour plots indicate that the fully developed and coherent vortex structures that we saw in the four previous flight conditions, namely primary and secondary vortices over the inner and outer wings, are not present in this flight condition. The convergence-divergence of skin-friction lines do show the confluence of vortical layers near the mid-span of the wing that likely separates and re-attaches inboard near the fuselage. If separation does occur, lift-off appears to be minimal. The flow does separate from the airdam/actuator-pod and a small vortex seems to develop. But flow does not separate from the leading edge of either the inner wing or the outer wing. Overall vortex-flow effects on the aircraft's performance at this flight condition is expected to me small.

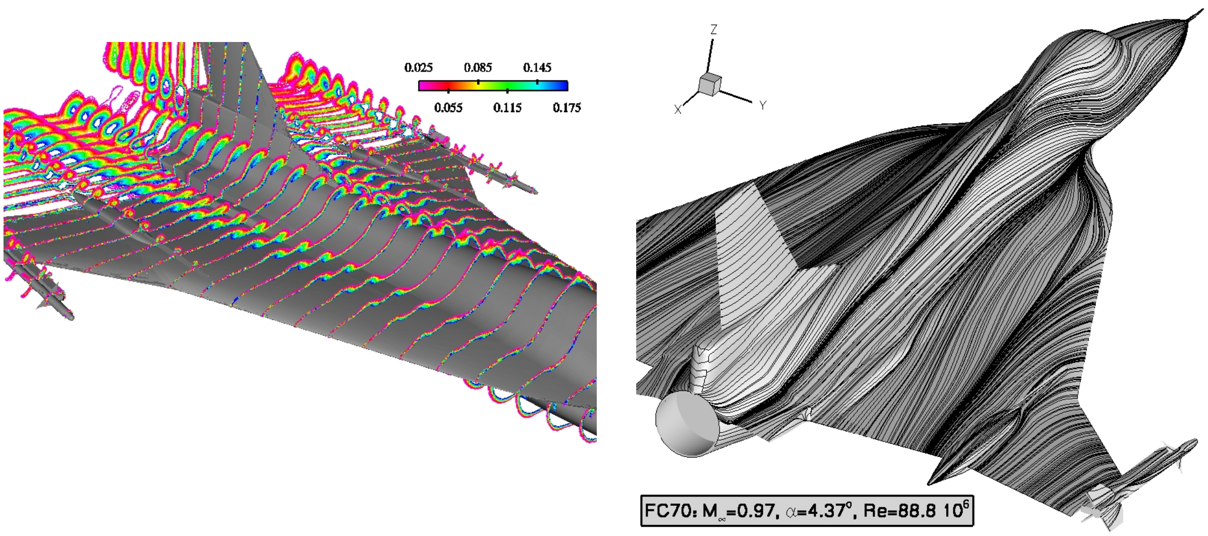

(a) **Sectional spanwise contours showing vortical layers over upper surface**

(b) **Skin friction lines over complete aircraft**

Figure 18. Vortical layers over upper surface for FC70: confluence of boundary layer towards mid-span wing but no substantial lift-off or development of coherent vortices a) iso-total-pressure contours, b) skin-friction lines, Boelens et al.[4]

On the other hand, at $M_\infty = 0.97$ the critical value of pressure coefficient is $C_p^* = -0.052$ so very small values of angle of attach will be sufficient to raise the suction pressure into the supercritical range, and the flow will be supersonic. Consequently shocks will appear when this flow must decelerate again to ambient conditions. This flight condition does indeed contain complex shock phenomena as illustrated in Fig 19 that shows surfaces of constant $M = 1$ which are colored by contours of total pressure. Part of the surface may be a sonic surface or may be a shock, depending on whether the flow is accelerating into the surface and decelerating out of it. In the latter case, the total pressure will vary rapidly across the surface. This fact can help in interpreting the figure.

Figure 19 suggests there are shock waves that start on the lower surface, drape over the leading edge and cover the entire upper surface. Keep this mental picture in mind when comparing the surface pressure values.

B. C_p Comparisons along Butt Line Sections

Similar to the previous four flight conditions, Figure 21 presents chordwise comparisons of the computed and flight-tested surface pressure coefficients C_p plotted along the butt-lines. Two long tick-marks are drawn on the vertical axis in each diagram representing the critical values of C_p^*, the lower one at -0.052 corresponding to $M_\infty = 0.97$ and the other slightly above it corresponding to $M_\infty = 0.95$, the value of the specific flight test. A general inspection of this figure prompts the overall comment that the computed data agree very well among themselves but differ substantially from the measurements, except at BL55 where all results are in good agreement. At BL55 there is a shock wave at approximately 5% chord due to the decelerating effect of the low sweep of the inner-wing fairing. There is another shock wave at about 30% chord of the upper surface. But notice that there also is a shock at 20% chord of the *lower* surface, seen in the computation. There are, however, no measured values at this location to confirm it. The shock pattern described by the computed results at BL55 is consistent with that shown in Fig 20.

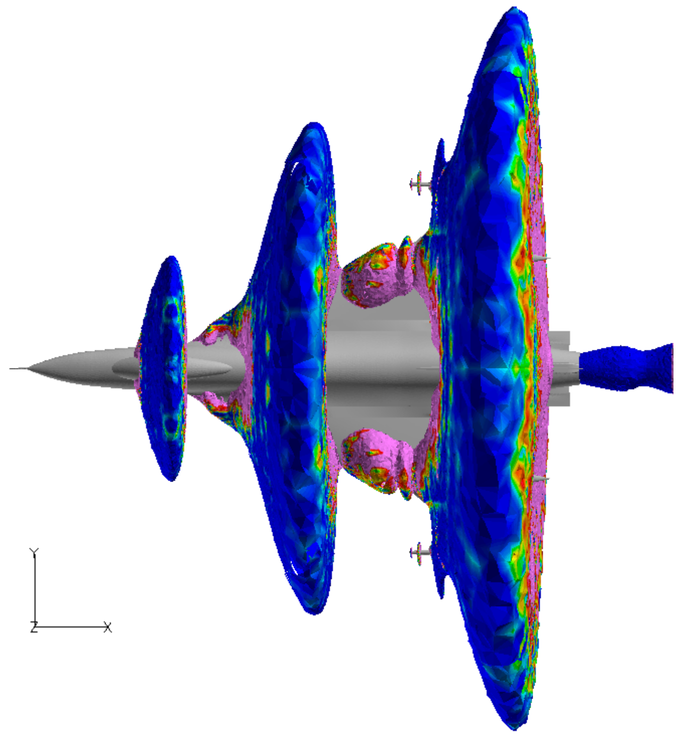

Figure 19. Shock topology in FC70. Iso-surfaces of Mach-1 colored by total pressure showing sonic surfaces and shock waves. Total pressure varies rapidly through shock wave, Davis et al.[13]

Along BL70 the computations agree with each other, but not with the measurements which are chaotic with no discernible pattern. The reasons for this is unknown, but there is reference to the leading-edge flap being deployed 9° during the test. The computed results show a shock on the upper surface at approximately 25% chord and a weaker shock on the lower surface near 15% chord, consistent with Fig 19. At BL80 the measured data is coherent, but it indicates a shock at 50% chord whereas the computed results show it at 20% chord. No apparent explanation for this disparity. At BL95 there is good agreement between computation and measurement, indicating a shock at about 10% chord of the upper surface. There is also an expansion at about 90% chord, over the trailing-edge flap.

The last two butt-lines, BL153.5 and BL184.5, are on the outer wing where the flow is influenced by the airdam, crank and missile, and differences begin to grow in the computed results especially in the aft part of the chord. At BL153.5 the measurements might suggest a shock just before 80% chord, in disagreement with the computations. At BL184.5 no shock can be discerned in either the measurements or the computations.

Figure 20 presents an attempt to synthesis the above comparisons by superposing computed isobars (in red) over the entire upper surface over those measured on the right-half wing (in black). The measured isobars are chaotic with no discernible pattern to them, the computed isobars are consistent with the shock topology in Fig 20.

C. C_p Comparisons along along Fuselage Stations

Lastly we turn to the spanwise plots of C_p in Fig 22. At FS300 the measurements indicate a shock around 60% span whereas the computed results show none. The explanation for this could be that the shock occurs further downstream in the measurements than in the computations, as evidenced in BL80. There are few measured data points and they agree well with the computations at least in the region of subsonic flow over the inboard half of the span. At FS375 we see supersonic flow around the airdam and the leading edge. The

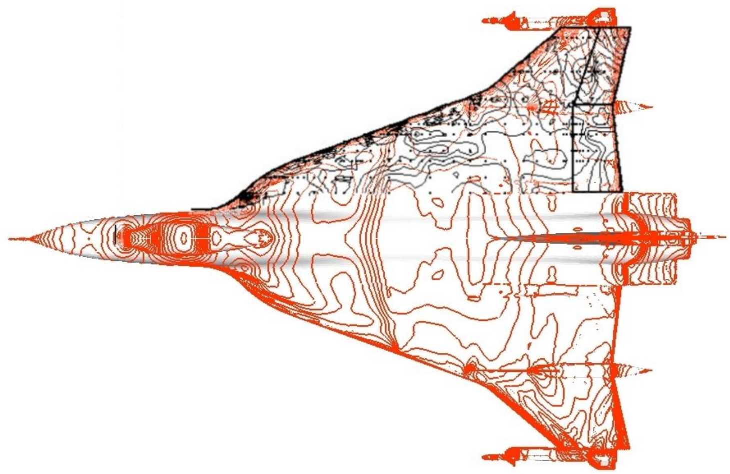

Figure 20. Comparison of computed (Goertz et al.[8]) and flight data (Lamar et al.[1]) C_p isolines, FC70. Computation in red, test in black

measurements might suggest a shock around 55% span. The computations agree with the measurements in subsonic flow but not in supersonic flow. The computed results show supersonic flow over the inboard part of the *lower* wing. At FS492.5 the computations indicate supersonic flow over the upper and lower surface, the measured data are few and scattered.

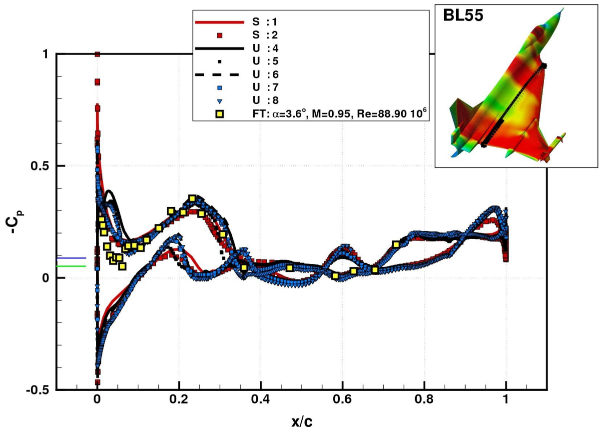

(a) **BL55**

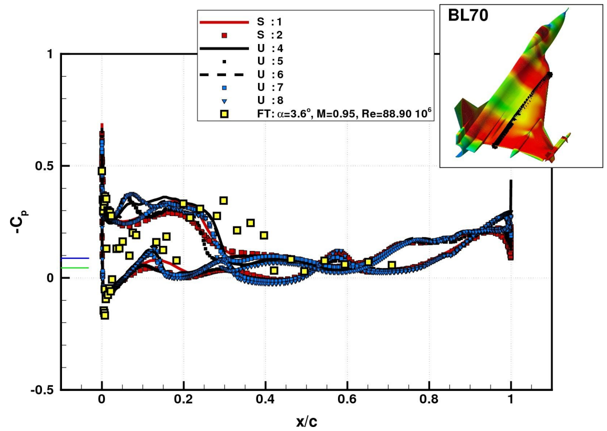

(b) **BL70**

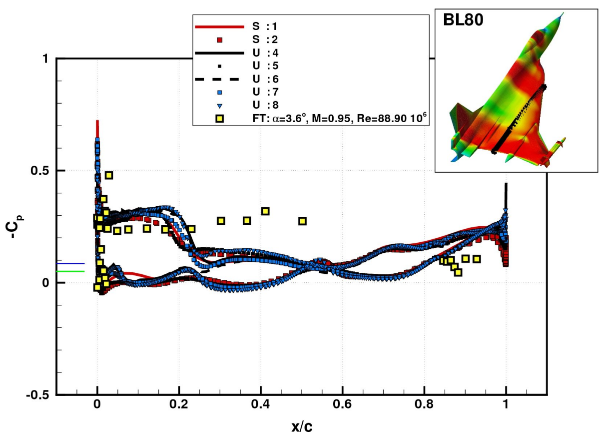

(c) **BL80**

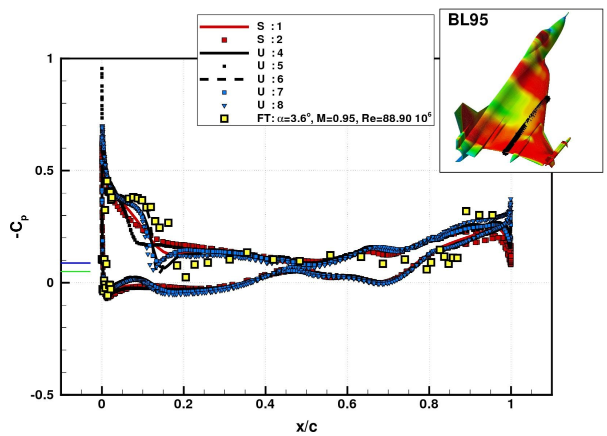

(d) **BL95**

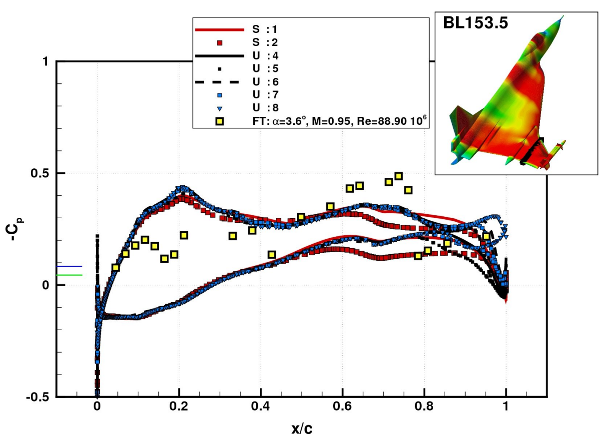

(e) **BL153.5**

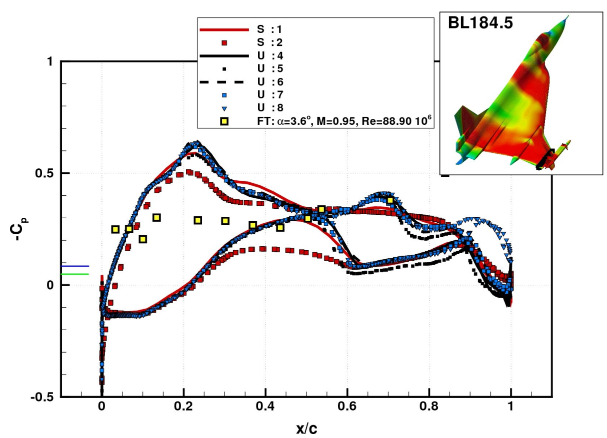

(f) **BL184.5**

1 - NLR, 2 - ULiv, 3 - NASA-S, 4 - KTH/FOI, 5 - EADS-MAS,
6 - UTSimC, 7 - NASA-U, 8 - USAFA, 9 - Boeing, 10 - LMAC

Figure 21. Chordwise comparison of computed and measured surface pressure coefficient along six butt-lines (BL) for case FC70: a) BL55, b) BL70, c) BL80, d) BL95, e) BL153.5, f) BL184.5

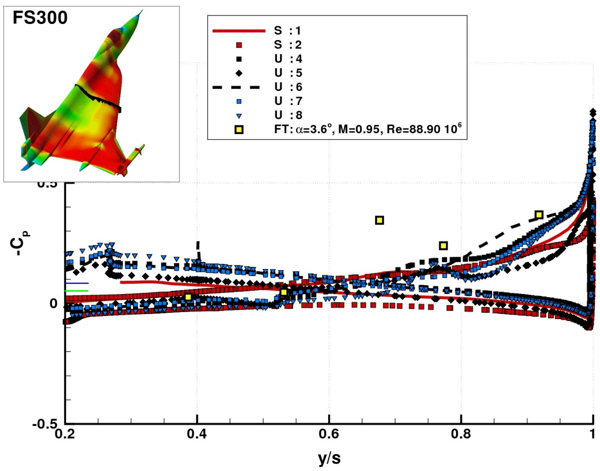

(a) **FS300**

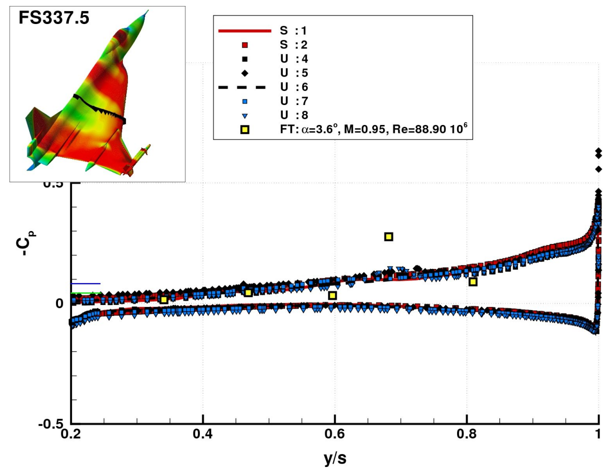

(b) **FS337.5**

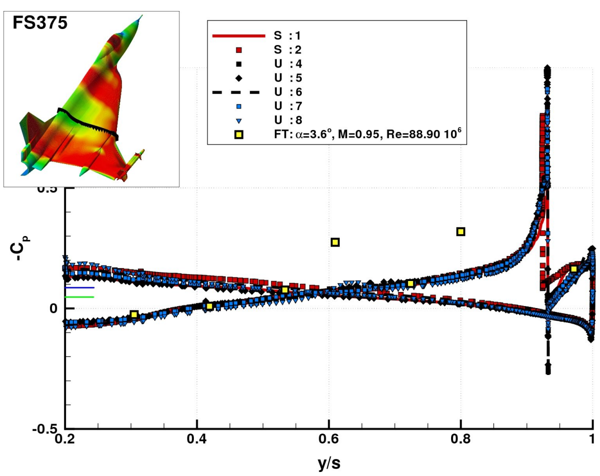

(c) **FS375**

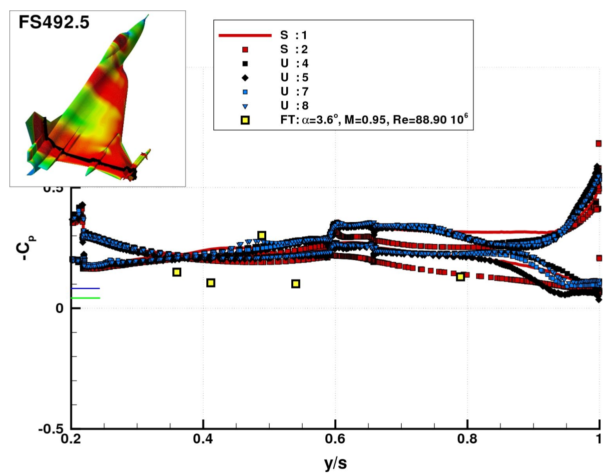

(d) **FS492**

1 - NLR, 2 - ULiv, 3 - NASA-S, 4 - KTH/FOI, 5 - EADS-MAS,
6 - UTSimC, 7 - NASA-U, 8 - USAFA, 9 - Boeing, 10 - LMAC

Figure 22. Spanwise comparison of computed and measured surface pressure coefficient along five fuselage-station lines (FS) for case FC70: a) FS300, b) FS337.5, c) FS375, d) 492.5

VI. Observations & Lessons Learned

We make some very initial remarks on the observations made on the comparison of results in the preceding sections, with regard to grids, turbulence models and unsteady modeling.

A. Grids & Grid Design

The standard structured grid Boelens[3] has generated the standard structured grid at the Netherlands National Aerospace Laboratory NLR using its new Cartesian grid mapping technique. NLR has developed reasonably semi-automatic grid generation tools as part of its ENFLOW CFD system. Most of these tools had become available just before CAWAPI and had only been applied to a simplified (no external loads) F-16 configuration. Despite CAWAPI being the first realistic case to which these tools were applied and bearing in mind that a limited experience with their use existed, it took only about six weeks to generate the complete grid which signifies the power of this tool. See the companion paper by Boelens et al.[3] for additional information on how the structured grid as well as the unstructured one was generated. Contributors NLR, ULiv and NASA-S used this grid.

The standard unstructured grid These are the origins of the standard unstructured grid. The NASA Langley Research Center, using the grid generation packages GridTool and VGRIDns, created a 3D all-tetrahedral viscous grid with 2,534,132 nodes, corresponding to 14,802,429 cells for a half-span full-scale model of the F-16XL-l (control surfaces not deflected). This grid was then converted to a hybrid grid in Cobalt-format at the USAFA using the commercial grid-management utility Blacksmith from Cobalt Solutions, LLC. Blacksmith reduced the cell count to a total of 11,928,103, corresponding to 2,535,842 nodes, by combining highly stretched tetrahedral cells into prismatic cells. The program generated 9 layers of prismatic cells, corresponding to 1,442,394 prisms. The reason the grid has only 9 layers is that pyramids would be needed as 'end caps' for layers that are not complete. Rather than adding another cell type it was decided to accepted 9 layers. The transition between the prismatic layers and the tetrahedral grid is very smooth. The surface of the half-span model of the F-16XL is discretized with 160,266 triangular elements. The upper surface grid is shown in Fig. 23(a) and 23(b).

Due to this need for prism layers it is commonly thought that unstructured grids lose accuracy in the boundary layer, but if the grid is properly generated with respect to the boundary-layer elements, just as accurate solutions are obtained with unstructured grids as with structured ones. Prism and hexahedral elements in the boundary-layer region are believed to be the best, but the use of tetrahedral elements is possible if one of the edges of the tetrahedral is aligned normal to the wall.

The resolution of the boundary layers requires the grid to be clustered in the direction normal to the surface with the spacing of the first grid point off the wall to be well within the laminar sublayer of the boundary layer. For turbulent flows, the first point off the wall should exhibit a y^+ value of less than 1.0. Here, the spacing of the first grid point normal to the solid wall is $5.0x10^{-6}$ m. Away from the wall, the spacing increases by a ratio of 1.2. Test simulations of FC19 show that an average value of y^+ of less then one and a maximum y^+ value of about two under the primary inner-wing vortex, demonstrating that the grid is fine enough at the wall boundaries. The engine duct is meshed all the way to the inlet duct exit plane. The nozzle is meshed from the engine mixing plane. Contributors KTH/FOI, NASA-U and USAFA used this grid.

The boundary conditions are symmetry, adiabatic wall for the surface of the aircraft, and characteristic variable freestream conditions for the far-field boundaries, which are located about 10 aircraft length (24 root chord lengths) away from the aircraft. The boundary conditions on the inlet duct exit plane and the mixing plane are pressure outlet and total states inlet, respectively. The corresponding propulsion conditions are given for the different flight conditions.

Adapted/tuned unstructured grids Instead of using the standard unstructured grid, contributors EADS-MAS, UTSimC, Boeing and LMAC choose to generate its own grid from scratch so that mesh adaptation, either automatic or by manual manipulation, could be applied to produce a resulting mesh that is refined to the solution and/or tuned to the solver to better capture the physics of the flowfield. Using automatic adaptation Fritz[9] began with an initial grid of 10M points and after refinement, the final adapted grids contained some 22M points with 30 prismatic layers over the surface. More details and figures of these adapted grids are not available to us at the time of writing. The reader is referred to the individual papers

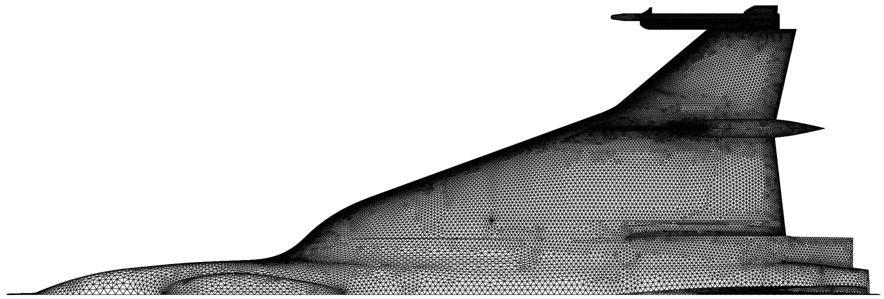

(a) **Symmetry plane of the hybrid grid showing the meshed inlet duct and nozzle**

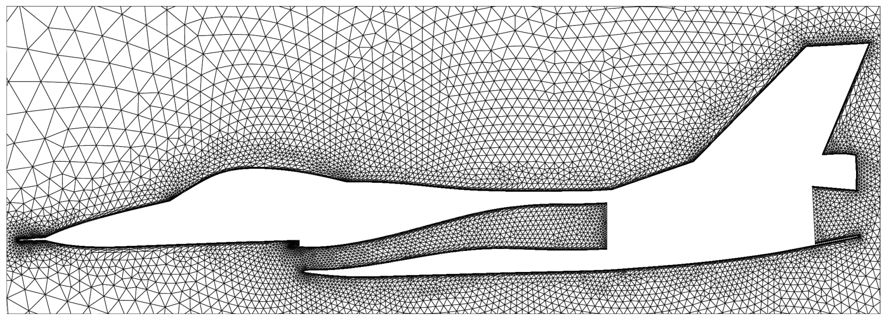

(b) **Symmetry plane of the hybrid grid showing the meshed inlet duct and nozzle**

Figure 23. Unstructured surface grid for the F-16XL-l half-span model (160,266 faces)

by Fritz,[9] Karman,[10] Michal[5] and Davis[13] for more information.

1. Mesh Commonality

At its start CAWAPI had a vision to run all calculations on two common meshes - one structured and one unstructured. As the project proceeded, most of the participants using unstructured meshes decided to use their own meshes suited to the needs of their codes. Perhaps the main motivation was the questionable quality of the results obtained on the common mesh. From that point of view it can be said that the idea of common mesh failed and that the time and effort to generate this mesh was wasted. Some results[9] even suggest that the mesh in today's CFD can be considered a part of the solution and that the initial idea of using a common mesh to control the truncation error when comparing the computed results of different CFD codes is becoming less viable.

However, there are several reasons why a common mesh, even if not used for the final results, does make a very important contribution. Most of the participants made their first runs on the common mesh, evaluated the results by comparing them to flight data and then made a decision whether to use this mesh for other flight conditions or to refine this mesh or to make a new mesh. Another reason for participants that do not have access to an advanced grid-generation tool, or the time to generate an advanced mesh, is that the common mesh provides a means for participation, i.e. it jump starts the solution process. Thus we see an extended role for the common mesh in today's collaborative projects. Perhaps the most important goal of using a common mesh in the future will not be for the controlled comparison of computations using the same mesh, but instead for distributing it among the project partners to enable them to get started quickly and then go on to produce their own high-quality grid tuned to their solver.

B. Turbulence Modeling Effects

1. Pressure Coefficient

Based on the KTH/FOI results, the differences due to turbulence models depends on the location on the aircraft and the angle of attack. At lower angles (FC7,FC46) the usual trend which can be detected is that the EARSM models, both with and without rotational corrections, are very similar. In most cases the SA model departs from other solutions usually at BL80 and higher. For these cases DES and DRSM did not bring improvement. Two locations are particularly interesting - the suction peaks in BL55 (Figure 24(a)), where at FC46 some models over-predicted the secondary vortex, both in the NASA and KTH/FOI results. These were usually non-linear two-equation models (NASA) or EARSM models (KTH/FOI). The second location where the differences between models are rather large is BL184.5 (Figure 24(b)) where the flow is affected by the vicinity of the AMRAAM missile and is presumably very chaotic.

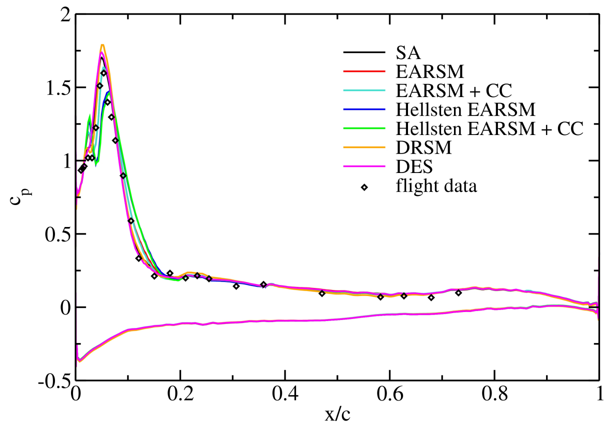

(a) **BL55**

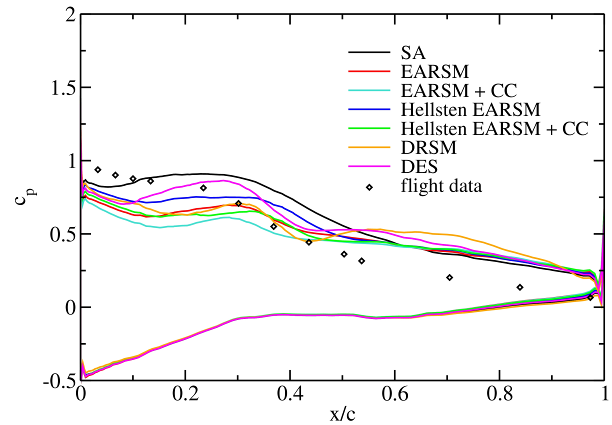

(b) **BL184.5**

Figure 24. C_p comparisons, different turbulence models, FC46, Goertz et al.[8]

At higher angle of attack (FC25), the differences between turbulence models grow larger. The Hellsten EARSM model with rotational corrections (KTH/FOI) showed rather good performance. At this conditions, DES brings an improvement in position of the primary vortex at BL184, see Fig 25.

At the transonic flight condition FC70, KTH/FOI was not able to obtain a solution with the SA model. There is however no visible difference in results from the different EARSM models with and without rotational corrections.

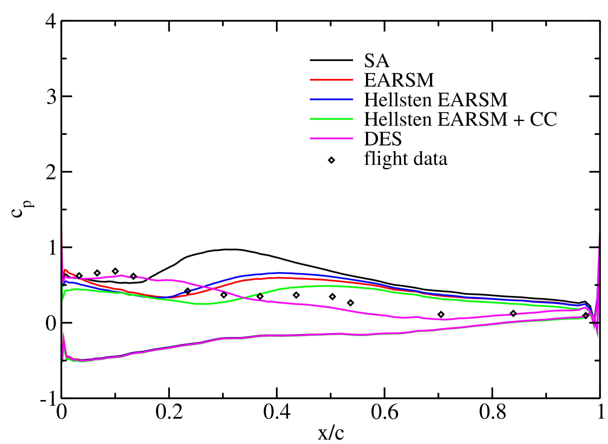

Figure 25. C_p comparisons, different turbulence models, FC25, BL184.5, Goertz et al.[8]

2. Skin-friction Coefficient

KTH/FOI observed differences in the values of C_f computed with different turbulence models. Again, the SA model departs quickly from other models, giving lower values of C_f under the primary peak and milder slopes. Results from all other models are rather close to each other. They differ in predicting the value of C_f under the primary vortex and generally fail to predict the slope of the measured C_f curve on the inner wing between the fuselage and the primary vortex.

3. *Velocity Profiles*

The velocity profiles in the boundary layer are in fairly good agreement with flight data. Again, the SA model departs somewhat from the solutions of the EARSM models.

4. *Conclusions: Modeling Effects*

Based mostly on observations of the KTH/FOI computations, the conclusion would be: the SA model is the model which had the poorest performance. Its predictability of flight data is usually very good in stations close to the fuselage and then it usually becomes worse going outboard. The predictions of the velocity profiles was fairly good. EARSM models usually yield good predictions and their results are consistent. DES modeling improves the flow solution at high angle of attack, at lower angle of attack its performance is similar to eddy-viscosity turbulence models.

No single model is best for all cases! The use of a particular turbulence model is perhaps motivated mostly by the confidence the user has with that particular model and the consistency of its results at different flight conditions rather then its optimum performance at one specific flight condition. For example, Steve Karman studied several different turbulence models in the process to determine the cause of disagreement with the flight data. After the study determined that grid resolution was the culprit, he ran all the cases with only one turbulence model, the two-equation k-epsilon, k-omega hybrid model.

C. Unsteady Flow Effects

Morton et al.[12] have focussed on investigating the possible unsteady effects at the various flight conditions. Carrying out time-accurate simulations require competent treatment of a number of factors. They point out several of these:

- *Determining the proper time-step size for resolving the desired unsteady structures.* They found that simply looking at the modal content of integrated forces/moments is not good enough when the flowfield is complex like that of the F-16XL (multiple vortex cores, etc.). They looked at time histories of pressure taps embedded along the main vortex core through the breakdown location in their simulations. A number of plots of the spectral-density estimates for the various tap locations are shown in their paper.[12]

- *How to time-average the time-accurate CFD data* This is necessary in order to compare it against experimental data (which because of the instrument is assumed to be averaged over a finite length of time). They have time-averaged results for FC7 over different time periods (i.e. number of time steps) and found a definite convergence trend.

  Morton et al.[12] carried out a number of time-accurate simulations of FC7 at a variety of time-step sizes ranging from 0.005 sec to 0.00005 sec (non-dimensional time-step sizes ranging from 0.068 to 0.00034). They concluded that a physical time-step size of 0.0005 sec is sufficient to capture the modal behavior of the primary vortex and developed a good rule-of-thumb that states: use a non-dimensional time-step size of approximately 0.01 for time-accurate simulations.

- *What are the max/min temporal values of flow quantities* For example the temporal oscillations in surface C_p over a specified number of iterations. They have produced the usual C_p plots but with "error bars" depicting the level of unsteadiness in the flow, Fig 26 presents one of them. Figure 26 shows that the surface pressure is reasonably steady over the inner wing (BL55), it is substantially unsteady over the outer wing where the interaction zone of the various vortices form a highly unsteady system (which makes sense). In fact for BL153.5 the temporal min/max range in the C_p is of the same size as the spread in the different steady contributions (see Fig 4).

VII. Progress Made in Modeling since NASA-TP[1]

A. Status of CFD Predictions Reported in the NASA-TP[1]

In Lamar et al.[1] flight and wind tunnel test data are presented and are compared with CFD predictions. The code CFL3D was used, which was developed at NASA Langley and is widely used in the United States.

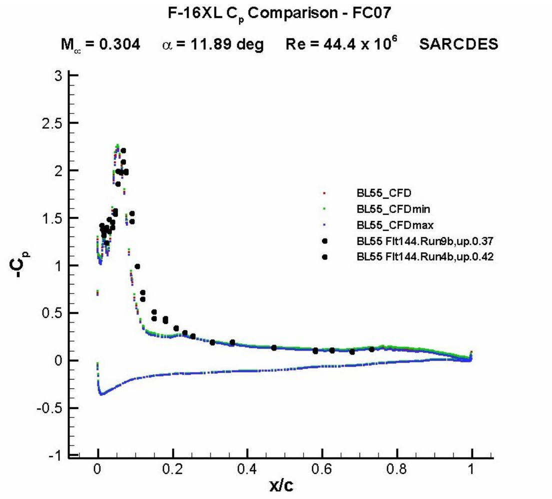

(a) **BL55**

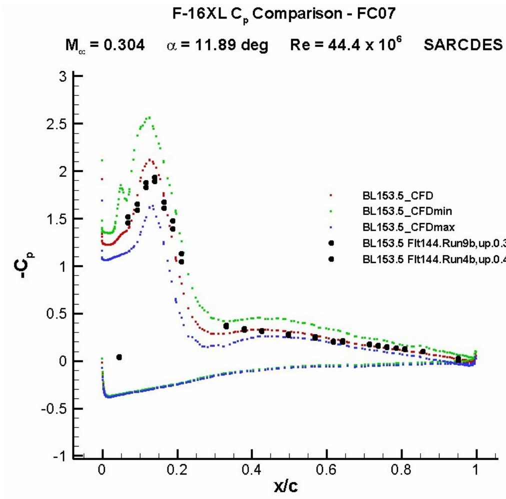

(b) **BL153.5**

Figure 26. Comparison measured C_p coefficient with computed: 1)time-averaged, 2)min temporal value and 3) max temporal value, FC7; a) BL55, b) BL153.5. (Morton et al.[12])

A patched multiblock grid was generated on a simplified half configuration of the F-16XL, with the intention to focus grid points on the wing to resolve vortices and shocks. The wing tip missile and launcher, and the vertical fin were removed, although the air dam was retained. The final grid had 1.37 million cells, with the first cell spacing set for the wind tunnel Reynolds number. The flight Reynolds number was computed using a wall function. The turbulence model used was Baldwin-Lomax with the Degani-Schiff modification for vortical flow. The calculations were run on the Cray C-90 and each steady calculation required around 24 hours. The convergence was stopped after the residual had been driven down 2-3 orders, which is unlikely to give full convergence. Finally, the commercial package Fieldview was used to visualise the vortices.

For the vortical flight conditions considered in AVT-113 the C_p distributions generally show better agreement inboard. However, suction peaks are under-predicted. One contribution to this is the coarseness of the grid. There were also significant discrepancies between the skin friction and boundary layer predictions and measurements. For FC70 (transonic case), good agreement was again obtained inboard, with very poor comparison with flight measurements outboard of the crank. A possible cause of this was suggested to be the uncertain deployment of the leading edge flaps and the ailerons. It was also stated that the convergence of the transonic case was more difficult.

B. Progress since the NASA-TP

Computing Power The computing power available to the participants in AVT-113 is one to three orders of magnitude larger than that available for the NASA-TP calculations. The codes used in AVT-113 all ran on distributed memory parallelism, with the exception of the NLR code which exploits a very high vector performance. The cost of computing has fallen to such an extent that many participants used local resources, whereas Lamar et al[1] relied on an allocation on a supercomputer.

Geometry Handling Emphasis in the working group was placed on retaining as much of the detailed definition of the aircraft as possible. A number of minor simplifications were made[3] but to a very large degree this goal was achieved. A number of partners were able to use their own grid generation tools to generate a grid around the extremely complex shape. It seems likely that the geometry simplifications in Lamar et al[1] were driven by the need to keep the number of grid points down.

Grid Generation Several AVT-113 partners used their own tools to generate grids around the complex F-16XL shape. The most direct comparison with Lamar et al[1] is with the structured grid generation of NLR. It is clear that the tools developed at NLR represent a major advance on what was available at the time of Lamar et al.[1] A significant development is the ability to generate unstructured grids for viscous flows through the exploitation of grown layers in the boundary layer. A number of codes were able to generate grids in a reasonable time. Finally, EADS-MAS made effective use of automatic grid adaption, the use of which is not currently as widespread as might have been expected.

Turbulence All participants in AVT-113 used turbulence treatments based on PDE's, in contrast to the algebraic model used in Lamar et al.[1] The simplest turbulence treatment used was one or two-equation turbulence models. Rotation corrections to Boussinesq based models seemed to allow good solutions without too much difficulty, to the extent that they could be described as routine. Some partners used Reynolds' Stress models, but without obvious benefit. Finally, some partners used DES.

Unsteadiness Some partners showed it is now possible to resolve Unsteady effects, showing significant unsteadiness downstream of the crank. The origins of this need further study, but could originate from an interaction of the inner and outer wing vortices, or an interaction between the inner wing vortex and the air dam.

Solver Discretisation and solution schemes have advanced less since Lamar et al.[1] The efficiency of the schemes was not really considered in AVT-113, but interesting information about the performance on grids required for such a complex geometry could be obtained in the future. The spatial accuracy of the codes has not improved noticeably since the time of Lamar et al.[1]

Visualization Possibly driven by improved computing, the visualization of solutions produced in AVT-113 far exceeded that shown in the NASA-TP. Visualization through iso-surfaces, surface streamlines and the automatic detection of vortex cores all effectively showed the behavior of the solutions, including unsteady effects.

Concluding Remarks

Although substantial differences are observed in the comparison of results from eight different CFD solvers compared with measurements, these solvers all functioned robustly on an actual aircraft at flight conditions with sufficient agreement among them to conclude that the overall objectives of the CAWAPI endeavor have been achieved. The result of this endeavor has identified that confidence level in these codes are to such a degree that they can be considered for use as a tool to assist in understanding performance measured in flight testing, to chart potential risk factors between competing design choices and to help in assessing flight-test data.

Several remarks follow from the observations of the comparisons made for the three categories of flight conditions studied, namely fully developed vortex flow at moderate angle of attack, strongly interacting vortex flow at high angle of attach and compressibility effects and shock waves at high transonic speed. The major development since Lamar et al.[1] is the use of grids of the required resolution, facilitated by advances in computing power. Turbulence treatments with no topology information required, and which overcome Boussinesq-assumption problems in vortical flows, have become readily available and were used routinely by all partners. Unsteady effects can now be resolved. Impressive grid generation codes have become widely available through advances in multiblock grid generation methods and the ability to generate unstructured grids for viscous flows. The physical modeling, steady or unsteady, and the grid resolution both contribute to the discrepancies observed in the comparisons with flight data, but at this time we cannot determine how much each part contributes to the whole.

Perhaps more disappointingly, discretisation methods have not advanced from the time of Lamar et al.,[1] i.e. the numerical methods used are second-order accurate. In particular, there would be advantages in high-order schemes for resolving vortices. Some success was achieved with grid adaption, although this was not as widely applied for the unstructured grid studies as might have been expected. Overall one can safely say that the technology readiness of CFD-simulation technology for the study of vehicle performance of e.g. the F-16XL has matured since 2001 such that it can be used today with a reasonable level of confidence in practical use.

Acknowledgment

The authors gratefully acknowledge the support provided by Lockheed Martin Aeronautics Company - Fort Worth in providing a refined IGES geometry file and the parameter values of a generic engine that were subsequently used by facet members in their CFD studies, and the geometrical work performed by Mr. Edward B. Parlette of Vigyan, Inc. in generating a series of unstructured, tetrahedral grids from the IGES file, with the last one known as the base grid. Special thanks also to Todd Michal of Boeing, Stefan Goertz of DLR, David McDaniels of USAFA, John Lamar of NASA and Steve Karman of UT Chattanooga for their valuable suggestions and kind assistance in the writing of the paper.

References

[1]Lamar, J. E., Obara, C. J., Fisher, B. D., and Fisher, D. F., "Flight, Wind-Tunnel, and Computational Fluid Dynamics Comparison for Cranked Arrow Wing (F-16XL-1) at Subsonic and Transonic Speeds," NASA/TP 2001-210629, NASA, February 2001.

[2]Lamar, J. E. and Obara, C. J., "Review of Cranked-Arrow Wing Aerodynamics Project: Its International Aeronautical Community Role," AIAA Paper 2007-0487, Presented at 45th AIAA Aerospace Sciences Meeting and Exhibit Reno NV January 8-11 2007, 2007.

[3]Boelens, O. J., Goertz, S., Morton, S., Fritz, W., and Lamar, J. E., "Description of the F16- XL Geometry and Computational Grids Used in CAWAPI," AIAA Paper 2007-0488, 45th AIAA Aerospace Sciences Meeting and Exhibit Reno NV January 8-11 2007, 2007.

[4]Boelens, O. J., Spekreijse, S. P., Sytsma, H. A., and de Cock, K. M. J., "Comparison of measured and simulated flow features for the full-scale F-16XL aircraft," AIAA Paper 2007-0489, 45th AIAA Aerospace Sciences Meeting and Exhibit Reno NV January 8-11 2007, 2007.

[5]Michal, T., Oser, M., Mani, M., and Ross, F., "BCFD Unstructured-Grid Predictions On The F-16XL (CAWAPI) Aircraft," AIAA Paper 2007-0679, Presented at 45th AIAA Aerospace Sciences Meeting and Exhibit Reno NV January 8-11 2007, 2007.

[6]Badcock, K. J., "Evaluation of Results from a Reynolds Averaged Multiblock Code Against F-16XL Flight Data," AIAA Paper 2007-0490, Presented at 45th AIAA Aerospace Sciences Meeting and Exhibit Reno NV January 8-11 2007, 2007.

[7]Elmiligue, A. A., Abdol-Hamid, K. S., and Massey, S. J., "PAB3D Simulations for the CAWAPI F-16XL," AIAA Paper 2007-0491, Presented at 45th AIAA Aerospace Sciences Meeting and Exhibit Reno NV January 8-11 2007, 2007.

[8]Goertz, S. and Jirasek, A., "Unstructured Steady/Unsteady Solutions with Edge for CAWAPI F-16XL at KTH/FOI," AIAA Paper 2007-0678, Presented at 45th AIAA Aerospace Sciences Meeting and Exhibit Reno NV January 8-11 2007, 2007.

[9]Fritz, W., "Hybrid Grid RANS Solutions For The CAWAPI F-16XL," AIAA Paper 2007-0492, Presented at 45th AIAA Aerospace Sciences Meeting and Exhibit Reno NV January 8-11 2007, 2007.

[10]Karman, S., Mitchell, B., and Sawyer, S., "Unstructured Grid Solutions of CAWAPI F-16XL by UT SimCenter," AIAA Paper 2007-0681, Presented at 45th AIAA Aerospace Sciences Meeting and Exhibit Reno NV January 8-11 2007, 2007.

[11]Lamar, J. E. and Abdol-Hamid, K. S., "USM3D Unstructured Grid Solutions for CAWAPI at NASA LaRC," AIAA Paper 2007-0682, Presented at 45th AIAA Aerospace Sciences Meeting and Exhibit Reno NV January 8-11 2007, 2007.

[12]Morton., S. A., McDaniels, D. R., and Cummings, R., "F-16XL Unsteady Simulations for the CAWAPI Facet of RTO Task Group AVT-113," AIAA Paper 2007-0493, Presented at 45th AIAA Aerospace Sciences Meeting and Exhibit Reno NV January 8-11 2007, 2007.

[13]Davis, M. B., Reed, C., and Yagle, P., "Hybrid Grid Solutions on the (CAWAPI) F-16XL Using Falcon v4." AIAA Paper 2007-0680, Presented at 45th AIAA Aerospace Sciences Meeting and Exhibit Reno NV January 8-11 2007, 2007.